

Chapter 7

Applications in Superconducting SIS Mixers and Oscillators: Toward Integrated Receivers

P. N. Dmitriev, L. V. Filippenko, and V. P. Koshelets

*Kotelnikov Institute of Radio Engineering and Electronics (IREE),
Mokhovaya Street 11, Building 7, 125009 Moscow, Russia*
pavel@hitech.cplire.ru, lyudmila@hitech.cplire.ru, valery@hitech.cplire.ru

Currently, Nb-based tunnel junctions are basic elements of most low- T_c superconducting electronic devices and circuits. In particular, the superconductor–insulator–superconductor (SIS) mixers that employ high-quality Nb-based tunnel junctions have the noise temperature limited only by the fundamental quantum value $hf/2k_B$ [1–13], where h is Planck's constant, f is frequency, and k_B is Boltzmann's constant. The SIS receivers are presently used in both ground-based and space millimeter and submillimeter radio telescopes. At higher frequencies, the lack of compact and easily tunable local oscillators (LO) motivates the direct integration of a superconducting local oscillator with the SIS mixer. A superconducting integrated receiver (SIR) [14–17] comprises on one chip all the elements needed for heterodyne detection. Being lightweight and having low power consumption, in combination with nearly quantum-limited sensitivity and a wide tuning range

Josephson Junctions: History, Devices, and Applications

Edited by Edward Wolf, Gerald Arnold, Michael Gurvitch, and John Zasadzinski

Copyright © 2017 Pan Stanford Publishing Pte. Ltd.

ISBN 978-981-4745-47-5 (Hardcover), 978-981-4745-48-2 (eBook)

www.panstanford.com

of the superconducting local oscillator, the SIR becomes a perfect candidate for many practical applications. In this chapter, an overview of the Nb-based tunnel junction's technology at Kotelnikov IREE in Moscow (as well as the SIR and the superconducting LO developments) is presented. By improving on the fully Nb-based SIR, we have developed and studied Nb–AlN–NbN circuits that exhibit an extended operation frequency range. Continuous frequency tuning for the phase-locked superconducting LO has been experimentally demonstrated in the range of 350–750 GHz. These achievements enabled the development of a 480–650 GHz integrated receiver for the atmospheric-research instrument TELIS (TErahertz and submillimeter Lmb Sounder) [18–21]. Further developments of the Nb-based SIS junction technology, along with examples of its laboratory applications, will be also presented.

7.1 Nb-Based Tunnel Junctions for Low-Noise SIS Receivers and Superconducting Oscillators

To realize a quantum-limited performance, the SIS tunnel junctions with a high current density, high energy gap, and extremely small leakage currents are required. In this section, the technological aspects for fabrication of high-quality Nb-based tunnel junctions with parameters required for low-noise SIS are discussed. The fabrication technology of the Nb–AlO_x–Nb tunnel junctions is based on the fact that a very thin Al layer can completely cover the base Nb electrode [22–24], somehow “planarizing” the column-like structure of the Nb film. This Al layer is subsequently oxidized and the top Nb electrode is deposited on the oxidized layer to form a so-called trilayer structure. The SIS tunnel junctions were fabricated from the trilayer structure by using the selective niobium anodization process (SNAP) [25] or the selective niobium etching and anodization process (SNEAP) [23, 26]. The stress, surface morphology, superconducting characteristics, and crystal structure of sputtered Nb films, as well as the surface coverage of thin Al layers deposited on Nb films with different sputtering parameters, were evaluated in order to judge their applicability for fabrication of high-quality Nb–AlO_x–Nb junctions [27–30].

7.1.1 Niobium Tunnel Junctions with an AlO_x Barrier

For low-noise operation, the SIS tunnel junctions with a small leakage current $I_1(V)$ under the gap voltage and minimal energy gap spreading δV_g are required. This is especially important for relatively low-frequency devices ($f \approx 100\text{--}300$ GHz), since δV_g has to be much smaller than the frequency quantum hf/e and the leakage current at a bias voltage of about $V_g - hf/2e$ determines the noise of the mixer. Any additional structure on the IVC of the junction considerably decreases the operation range of the mixer. According to the procedure described above, a thin Al layer covers the Nb base electrode [22, 23]. As a consequence, a residual Al layer appears between the Nb and the isolator barrier, and the tunnel structure is Nb/Al/ AlO_x /Nb. It results in suppression of the Nb gap and the appearance of the so-called knee structure due to the proximity effect. A study of the knee's dependence on the thickness of the base Nb electrode and the additional Al layer was performed [31]; the experimental results were compared with numerical calculations based on the microscopic theory of the proximity effect.

The SIS tunnel junctions were fabricated [31] by using SNEAP on the crystalline Si substrates covered by a buffer layer of Al_2O_3 ($d = 80$ nm). A trilayer structure, Nb-Al/ Al_2O_3 -Nb, was deposited in a single vacuum run by using DC magnetron sputtering for both Nb and Al films ($P_{\text{Ar}} = 1 \cdot 10^{-2}$ and $5 \cdot 10^{-3}$ mbar; the deposition rate was approximately 2 and 0.2 nm/s for Nb and Al, respectively) [32]. The substrates were thermally attached to the holder under temperature control. Pure oxygen at an appropriate pressure was used for the formation of the tunnel barrier (oxidation temperature 300 K, time = 20 min). The SIS junction area was defined by RIE followed by anodization; the thermally deposited SiO layer of about 270 nm was used as an insulator.

According to the Werthamer tunnel theory, the IVC of the Nb-Al/ Al_2O_3 -Nb (S-S'-I-S) tunnel junction depend on the quasiparticle density of states (DOS) in the S' layer (Al). The DOS can be calculated on the basis of the microscopic proximity effect model for S-S' bilayers [33]. The model assumes a short electron mean free path (dirty limit conditions) in both S (Nb) and S' (Al) materials, resulting

in the following parameters:

$$\gamma = \frac{\rho_s \xi_s}{\rho_{s'} \xi_{s'}^*} = \sqrt{\frac{D_{s'} N_{s'}(0)}{D_s N_s(0)}}, \gamma_B = \frac{R_B}{\rho_{s'} \xi_{s'}^*}.$$

Here, $\xi_s = \sqrt{D_s/2\pi T_{cs}}$, $\xi_{s'}^* = \sqrt{D_{s'}/2\pi T_{cs}}$, $D_{s,s'}$, $\rho_{s,s'}$, and $N_{s,s'}(0)$ are the coherence lengths, the diffusion coefficients, the normal state resistivities, and the electronic densities of states in the normal states of S and S' metals, T_{cs} is the critical temperature of S metal, and R_B is the product of the resistance of the S-S' boundary and its area. The best fit with the experiment gave [31] the following set of parameters: $\xi_{Nb} = 15$ nm, $\xi_{Al} = 40$ nm, $\gamma = 0.3$, and $\gamma_B = 1$. Calculations in the model above show that the DOS in the S' layer has an energy gap of $\Delta_g < \Delta_{Nb}^{bulk}$ with a large weight of filled subgap states within the energy range $\Delta_g < E < \Delta_{Nb}^{bulk}$. That leads to the appearance of the knee structure on the IVC.

The definition of the knee value is illustrated in Fig. 7.1a [31]. The knee current I_k is defined as the point of maximum deflection of the IVC from the R_n line. I_k is normalized to the quasiparticle current jump I_g at the gap voltage V_g . The value of I_g is evaluated as a current at V_g between the lines of R_n and leakage resistance R_j . The value of V_g is determined at the crossing of the bisector between R_n and R_j with the measured IVC (see Fig. 7.1a).

The experimentally measured IVCs at different thicknesses of the base Nb electrode for $d_{Al} = 9$ nm are presented in Fig. 7.1b, and the currents are normalized to $I(4$ mV). The values of the knee determined from both theoretical and experimental curves, as well as the measured values of V_g , are listed in Table 7.1 [31].

Table 7.1 Parameters of Nb-AlO_x-Nb junctions (area $A = 7200 \mu^2$) for $d_{Al} = 9$ nm [31]

| d_{Nb} , nm | I_k^*/I_g^* (theory for $d_{Al} = 8$ nm) | I_k/I_g | V_g , mV |
|---------------|--|-----------|------------|
| 35 | 0.04 | 0.055 | 2.75 |
| 50 | 0.85 | 0.075 | 2.77 |
| 75 | 0.145 | 0.105 | 2.79 |
| 100 | 0.185 | 0.17 | 2.82 |
| 150 | 0.245 | 0.195 | 2.84 |
| 200 | 0.285 | 0.245 | 2.86 |
| 350 | 0.325 | 0.21 | 2.86 |
| 500 | 0.325 | 0.225 | 2.86 |

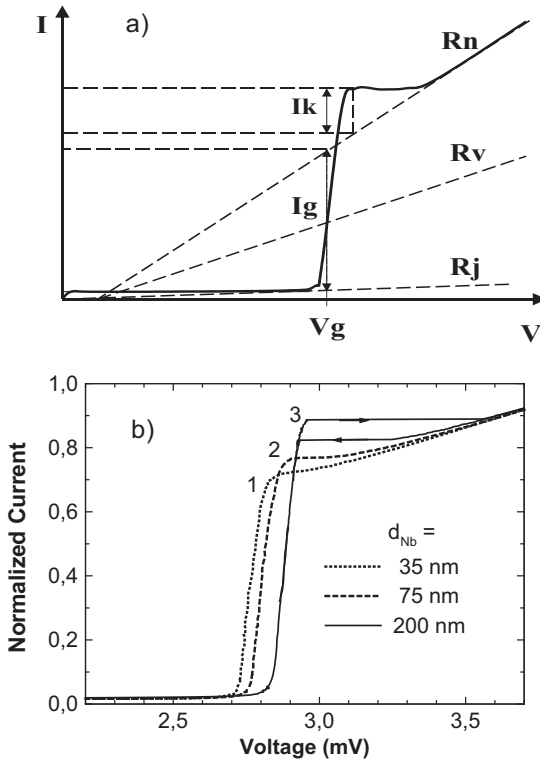


Figure 7.1 (a) Definition of the main parameters for the model SIS IVC. (b) Experimentally measured IVCs at $d_{Al} = 9$ nm for three different thicknesses of the base electrode. Reproduced with permission from Dmitriev et al. [31].

The normalized knee value $K^{Nb} = I_k(d_{Nb})/I_k(200 \text{ nm})$ is shown in Fig. 7.2. One can see that the experimental dependence coincides well with the theory up to $d_{Nb} = 200$ nm. At further increase of the Nb thickness, the surface morphology of the sputtered Nb films changes considerably [29]. As a result, the Al layer is not uniform and the measured knee (averaged over the junction area) is lower than the calculated one.

To avoid the morphology effect, a thin Nb base electrode ($d_{Nb} = 50$ nm) was used to study the knee’s dependencies on the Al thickness. The experimental IVCs for different Al thicknesses are shown in Fig. 7.3 [31]. It should be noted that the Al thickness decreased with oxidation; therefore, 1 nm was subtracted from the initial value in the calculations (see Fig. 7.2). The obtained data are summarized in Table 7.2.

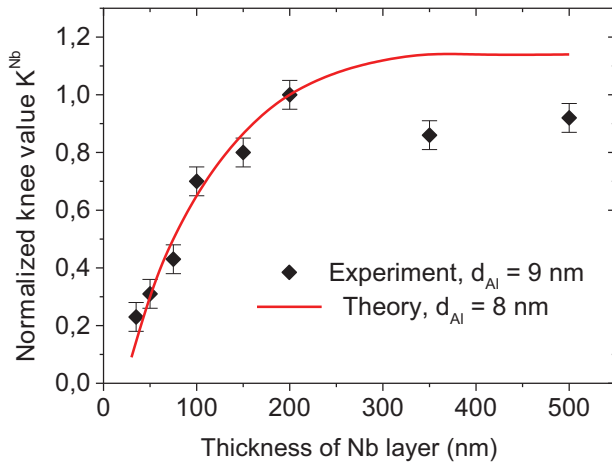


Figure 7.2 Calculated and measured values of the knee (normalized to the value at $d_{Nb} = 200$ nm) versus the thickness of the Nb base electrode. Reproduced with permission from Dmitriev et al. [31].

Table 7.2 Parameters of Nb–AlO_x–Nb junctions ($A = 1700 \mu^2$) for $d_{Nb} = 50$ nm [31]

| d_{Al} , nm | I_k^*/I_g^* (theory) | I_k/I_g | V_g , mV |
|---------------|------------------------|-----------|------------|
| 2 | 0 | – | – |
| 3 | 0.016 | 0 | 2.86 |
| 4 | 0.031 | 0.01 | 2.85 |
| 5 | 0.041 | 0.02 | 2.84 |
| 6 | 0.05 | 0.03 | 2.83 |
| 7 | 0.056 | 0.04 | 2.81 |
| 8 | 0.060 | 0.05 | 2.78 |
| 9 | 0.062 | 0.07 | 2.77 |
| 10 | 0.065 | 0.085 | 2.73 |
| 15 | 0.07 | 0.115 | 2.66 |

The SIS junctions with a thin Nb base electrode have almost ideal IVCs but are not suitable for high-frequency application since $d_{Nb} < \lambda_L^{Nb} = 90$ nm, which considerably increases the inductance of the microwave elements. To overcome this problem, an additional Al

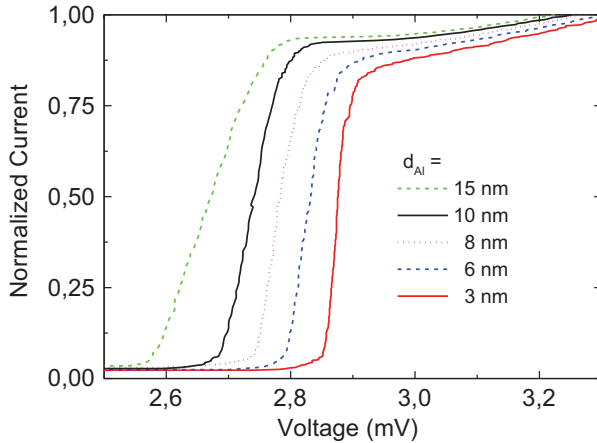


Figure 7.3 Experimentally measured IVCs at $d_{\text{Nb}} = 50$ nm for five different thicknesses of the Al layer. Reproduced with permission from Dmitriev et al. [31].

layer was introduced in the Nb base electrode to realize a “knee-free” IVC for a reasonably thick base Nb [31]. The introduction of an additional Al interlayer into Nb/Al/AlO_x/Nb structures leads to a steeper IVC and disappearance of the knee structure. The reason is that with the introduction of such a layer, the order parameter in a thin Nb–Al bilayer near to the barrier becomes spatially homogeneous, and thus the density of states in this bilayer becomes BCS-like, with a smaller energy gap. The experimental IVC for Nb/Al^{add}/Nb^{add}–Al₂/AlO_x–Nb structure is shown in Fig. 7.4.

As a result of Nb–AlO_x–Nb technology optimization and extensive analysis of the SIS receiver designs, a number of low-noise receivers have been designed and tested [6, 15]. The results of a quasi-optical 500 GHz SIS receiver are presented below [6]. The receiver consists of a double dipole antenna SIS mixer, with integrated tuning elements. It was designed as a reference system to measure the ultimate performance of an integrated receiver [4, 5]. The tuning circuit consists of an end-loaded stripline connected to the double dipole antenna via a matching stripline transformer [6, 15]. The SIS junction is an Nb–AlO_x–Nb junction with an area of 1.5 μm² and a

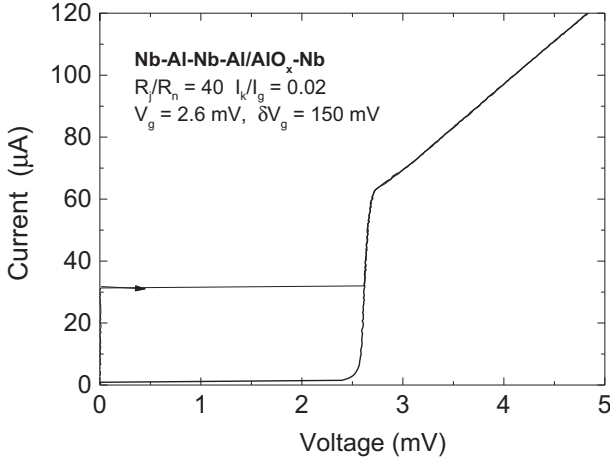


Figure 7.4 The IVC of the Nb/Al^a/Nb^a-Al/AIO_x-Nb junction at the thickness of the additional Al layer $d_{Ala} = 5$ nm and $d_{Nba} = 50$ nm. Reproduced with permission from Dmitriev et al. [31].

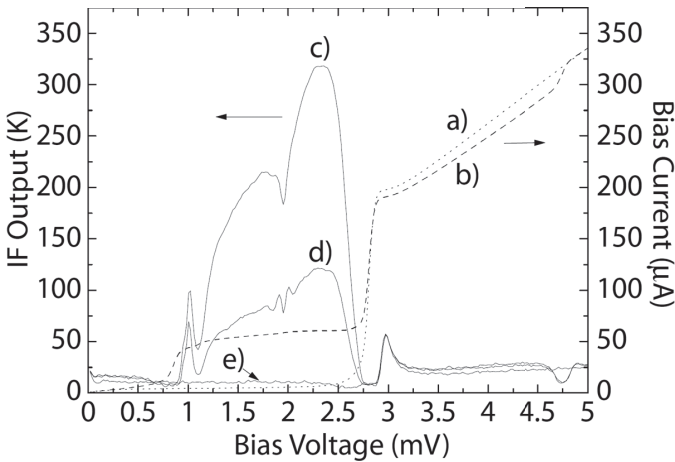


Figure 7.5 $I-V$ curves and IF output of the receiver. (a) Unpumped $I-V$ curve. (b) Pumped $I-V$ curve, identical for hot and cold loads. (c) IF output for a 295 K load (at optimal LO power). (d) The same as in (c) for a 78 K load. (e) IF output for zero LO power [6].

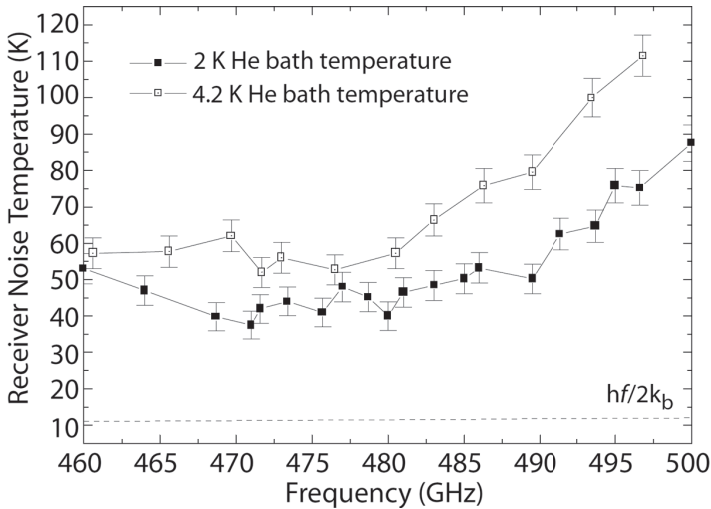


Figure 7.6 DSB receiver noise temperature for two different temperatures, uncorrected for the beam splitter. For comparison, the photon-noise floor of $hf/2k_B$ is included (represented by the dashed line) [6].

normal resistance of $R_n = 14 \Omega$; $R_i/R_n = 30$. The Josephson effect is suppressed by an integrated magnetic field control line. The receiver chip ($4 \times 4 \times 0.5 \text{ mm}^3$) is mounted on a silicon elliptical lens covered with an antireflection coating. A back reflector is mounted behind the antenna. The measured unpumped and pumped junction I - V curves, as well as the dependence of the IF output power on bias voltage, are shown in Fig. 7.6 [6]. The measured double-side-band (DSB) receiver noise temperature vs. the LO frequency is presented in Fig. 7.6 [6] and must be compared with the dashed line that indicates the photon noise limit $hf/2k_B$, with $hf/2$ being the photon energy. The best noise temperature, uncorrected for the beam splitter, of $40 \pm 3 \text{ K}$ was measured at 471 GHz. This is only approximately three times the zero-point fluctuation's noise level of 11.4 K.

7.1.2 Niobium-Based Tunnel Junctions with AlN Barrier

To realize the ultimate performance of the SIS mixers at sub-THz frequencies, tunnel junctions with very high tunnel barrier transparencies are required. Unfortunately, there is a limit for the

increasing of the AlO_x barrier transparency (of approximately 10–15 kA/cm^2); at a higher current density, abrupt degradation of the junction's quality takes place. The idea of utilizing SIS tunnel junctions for heterodyne mixing at THz frequencies has received remarkable support due to developments of Nb–Al–AlN–Nb tunnel junctions with very high current densities of up to 100 kA/cm^2 . That corresponds to low $R_n S$ values down to $2 \Omega \cdot \mu\text{m}^2$ (where R_n and S are junction the normal-state resistance and area, respectively) [34–38].

We produce Nb–Al–AlN–Nb tunnel junctions [39] in an oil-free UHV sputtering system with a base pressure of 10^{-6} Pa, which is provided by a combination of turbo-molecular and cryogenic pumps. This system is equipped with 5-inch DC and RF magnetron sources, an ion gun, and a grounded water-cooled substrate table. Wafers are fixed to the copper chucks using vacuum grease and are attached to the substrate table. The Nb–AlN–Nb junction fabrication procedure [39] follows the well-known recipe for conventional Nb– AlO_x –Nb junction production, and is described elsewhere [31]. The only difference in our case is the substitution of an oxidation step by a nitridation one. As in the case of the conventional Al oxide process, we deposited Nb and Al thin films using DC magnetron sputtering in an Ar atmosphere with a working gas pressure of 1 Pa. The dielectric layer for junction insulation consists of 250 nm SiO_2 , defined in a self-aligned lift-off procedure. The wiring layer is defined by lift-off.

It is well known that by using a simple exposure of sputtered Al surface in an N_2 atmosphere, one cannot acquire a continuous AlN layer of sufficient thickness to be used as a tunnel barrier [35]. Several successful attempts of Al nitridation have been made using a glow discharge in a nitrogen atmosphere [35–38]. Following this idea, we grew an AlN tunnel barrier immediately after Al deposition by using RF magnetron discharge. Samples were attached to the grounded substrate table and maintained at 20°C . To obtain a density of nitrogen ions capable of producing an AlN tunnel barrier, the sample holder was positioned directly above a five-inch Al magnetron RF source with a holder-source distance of 14 cm. The electrical scheme of the nitridation process is presented in Fig. 7.7. We initiated a plasma discharge using a very small power density of

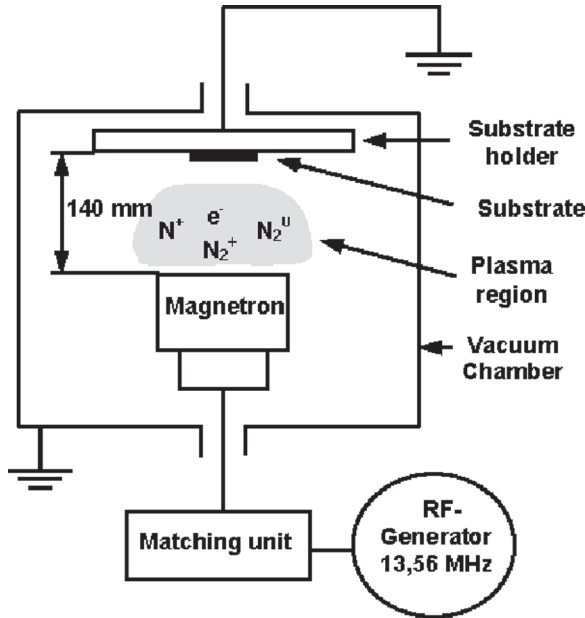


Figure 7.7 The electrical scheme of the nitridation process. Reproduced with permission from Dmitriev et al. [39].

0.5–0.75 W/cm². The nitrogen pressure was kept constant at 4.5 Pa. The total duration of the nitridation process varied within the range of 100–300 seconds. The use of such conditions, the small power, large source-sample distance, and dense plasma, permitted us to avoid both exposure of the samples to an energetic flux of ions and significant sputtering of the Al target during AlN growth.

A set of Nb–AlN–Nb junction *IV* characteristics is presented in Fig. 7.8. The critical current is suppressed by a magnetic field. The $R_n S$ value changes from 24 $\Omega \cdot \mu\text{m}^2$ for the curve (a) to 0.9 $\Omega \cdot \mu\text{m}^2$ for the curve (d). The increase of the subgap leakage follows the increase of the critical current density. Moreover, a self-heating in the junctions can be clearly seen in this figure. It causes both gap voltage reduction and back bending of the gap singularity. Figure 7.8b presents the *IV* characteristic of an Nb–AlN–Nb junction exposed to the nitrogen plasma for 300 seconds at 60 W of RF power. This junction with low $R_n S$ of 10 $\Omega \cdot \mu\text{m}^2$ demonstrates

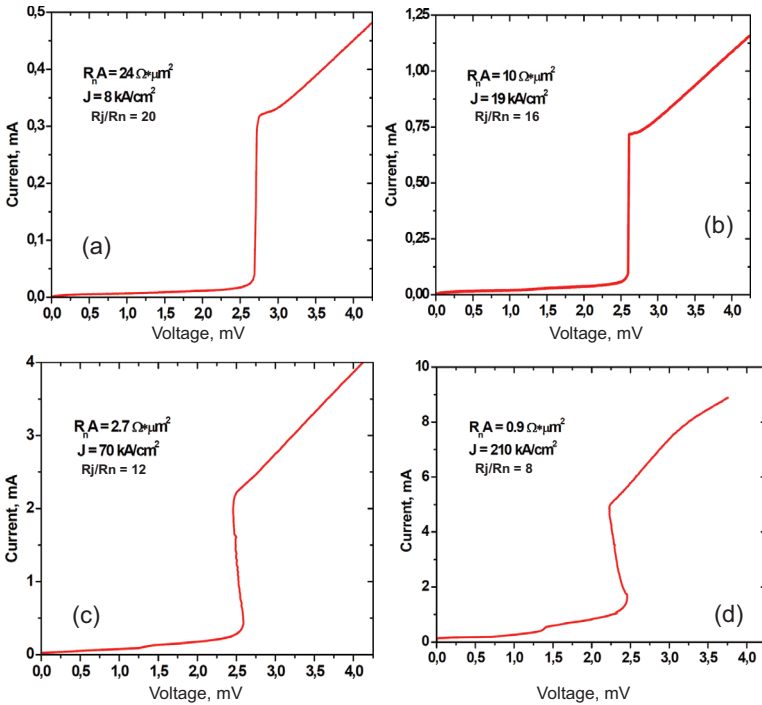


Figure 7.8 IVCs of Nb-AlN-Nb junctions with (a) $24 \Omega \cdot \mu\text{m}^2$, (b) $10 \Omega \cdot \mu\text{m}^2$, (c) $2.7 \Omega \cdot \mu\text{m}^2$, (d) $R_n S = 0.9 \Omega \cdot \mu\text{m}^2$; the critical current is suppressed by the magnetic field. Reproduced with permission from Dmitriev et al. [39].

excellent tunnel characteristics with $R_j/R_n = 16$. From other *IV* curves presented in Fig. 7.8 it is clear that the $R_n S$ value can be easily lowered down to 5–7 without significant degradation. Dependences of the junction quality parameter R_j/R_n on tunnel current density for Nb/ AlO_x /Nb junctions [39] are shown by asterisks in Fig. 7.9.

The implementation of an AlN tunnel barrier in combination with a NbN top superconducting electrode is expected to give a significant improvement in SIS THz mixer performance. To explore this idea we produced an Nb–AlN–NbN tunnel junction. NbN was deposited by DC reactive magnetron sputtering at ambient temperature with 1.8 W/cm^2 power density using Ar + 9% N_2 gas mixture. Otherwise the fabrication procedure was the same as described above for Nb–AlN–Nb junctions. The *IV* characteristic of this junction is presented

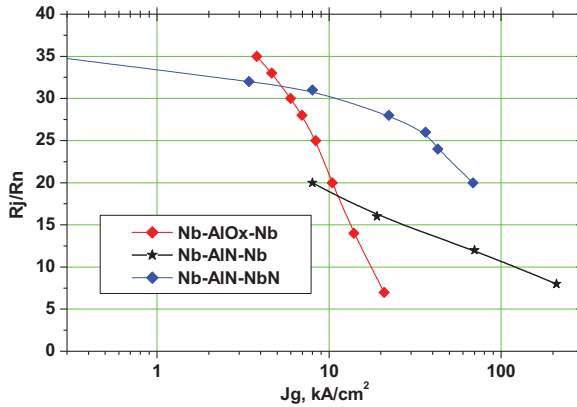


Figure 7.9 The dependencies of the R_j/R_n ratio vs. tunnel current density J_g for junctions fabricated at IREE using different techniques. Reproduced with permission from Dmitriev et al. [39].

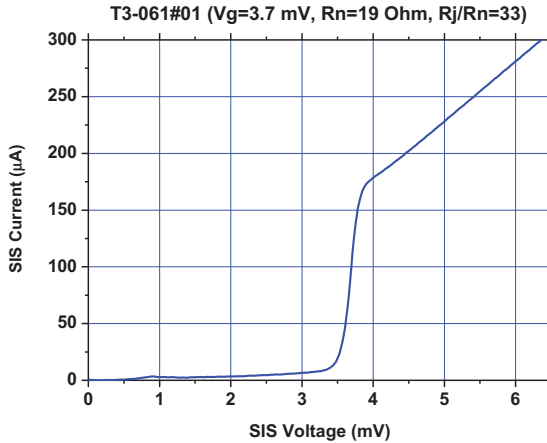


Figure 7.10 IV characteristic of the Nb-AlN-NbN junction ($S = 2 \mu\text{m}^2$, $V_g = 3.7 \text{ mV}$, $R_n S = 37 \Omega \cdot \mu\text{m}^2$, $J_g = 6.5 \text{ kA/cm}^2$); the Josephson supercurrent is suppressed by the magnetic field [40].

in Fig. 7.10. $R_n S = 100 \Omega \cdot \mu\text{m}^2$, $R_j/R_n = 32$, and the gap voltage is 3.7 mV. From this value and the voltage of the singularity corresponding to the difference of the superconducting gaps of the junction contacts $V_\delta = (\Delta_{\text{NbN}} - \Delta_{\text{Nb}})/e = 0.9 \text{ mV}$ we can estimate

the gap voltage of our NbN film as $V_g^{\text{NbN}} = 2.3$ mV. The dependency of the ratio of subgap to normal state resistance (R_j/R_n) vs. tunnel current density (J_g) for different types of the Nb-based junctions fabricated at IREE is presented in Fig. 7.9. One can see that the Nb-AlN-NbN junctions have very good quality at high current densities that is important for implementation in THz mixers.

High-quality Nb-AlN-NbN tunnel junctions were successfully used for development of the superconducting local oscillators and fully integrated superconducting receivers (see Sections 7.2 and 7.3). These junctions were also employed [41] to upgrade the 790–950 GHz CHAMP+ heterodyne array receiver [42] for the APEX (Atacama Pathfinder EXperiment) telescope [43]. The frequency of 950 GHz corresponds to a 3.9 mV photon step, which exceeds the V_g of “classical” SIS junctions with Nb electrodes ($V_g = 2.8$ mV, or even lower for extremely high current density junctions). Consequently, the voltage range available for the SIS mixer’s operation is considerably wider for the Nb-AlN-NbN mixers as compared to the Nb ones. An additional interest is to gain experience with high-gap mixer technology for later use at frequencies above 1 THz, for example, in the Millimetron project [44] in the 950–1150 GHz range.

In order to make a wide band receiver, twin SIS junctions [45, 46] (each with an area of $0.5 \mu\text{m}^2$) were used, which were coupled by a waveguide probe to the E field of a rectangular waveguide of $300 \times 75 \mu\text{m}$ (Fig. 7.11). Due to the high current density of the

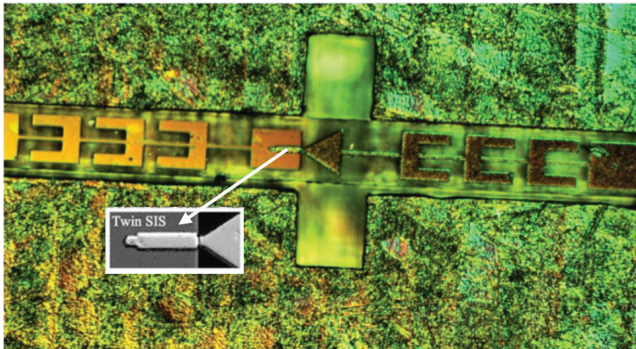


Figure 7.11 Photo of the SIS mixer (including the waveguide probe and filter structure) installed in a waveguide. The central part, with a SIS twin junction, is magnified [41].

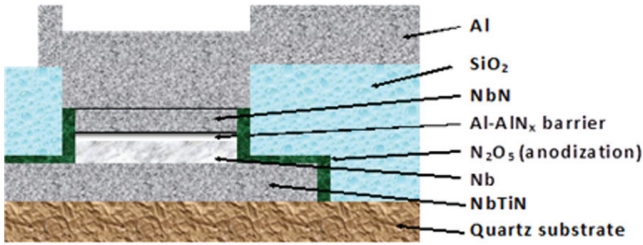


Figure 7.12 Cross section of the Nb/AlN/NbN tunnel junctions incorporated into a microstrip line consisting of a 300 nm thick bottom electrode (ground plane) made of NbTiN and a 500 nm thick top electrode made of Al.

produced AlN barrier; the lower R_n gives a higher $1/R_n C$ ratio for the junctions (C being the junction capacitance), thus providing a wider receiver band. The design of the tuning structure and waveguide mount is conceptually similar to the original design of the CHAMP+ high-band devices. The SIS junctions were embedded in a $4.5 \mu\text{m}$ wide microstrip line with a $6.5 \mu\text{m}$ interjunction distance, and coupled to the antenna by a $7 \times 27 \mu\text{m}$ impedance transformer tuned for the high current density junctions.

The SIS mixer was based on high critical current density Nb/AlN/NbN tunnel junctions incorporated into a microstrip line consisting of a 300 nm thick bottom electrode (ground plane) made of NbTiN and a 500 nm thick top electrode made of Al [7]. The microstrip electrodes were separated by a 250 nm SiO_2 isolator (see Fig. 7.12). The Nb layer of the SIS junction was deposited onto the NbTiN film, while the NbN layer was in contact with the Al top electrode. First, an NbTiN film was deposited onto a fused quartz substrate at room temperature, using DC sputtering with an NbTi target in a nitrogen atmosphere. For the NbTiN film, the critical temperature T_c was measured to be 14.1 K, and the room temperature resistivity was estimated to be $85 \mu\Omega \cdot \text{cm}$. The geometry of the ground electrode was determined by a reactive ion etching (RIE) process. The tunnel junctions were fabricated from an Nb/AlN/NbN trilayer [40] with a normal state resistance–area product $R_n A = 7 \Omega \cdot \mu\text{m}^2$, which corresponds to a current density of $J_c = 30 \text{ kA}/\text{cm}^2$; the Nb and NbN layers had thicknesses of 100 nm. An AlN tunnel barrier was grown immediately after deposition onto a 7 nm Al layer using an RF magnetron discharge. The samples were

attached to the grounded substrate table maintained at 20°C, which was positioned directly above a 5-inch Al magnetron RF source with a holder-source distance of 14 cm. For fabrication of the high current density trilayer, we initiated a plasma discharge using a power density of 0.7 W/cm² at a nitrogen pressure of 4.5 Pa; the nitridation time was approximately 40 seconds. Afterwards, the NbN was deposited by DC reactive magnetron sputtering at an ambient temperature, with 1.8 W/cm² power density using an Ar + 9% N₂ gas mixture. Circular-shape junctions with an area of approximately 0.5 μm² were defined by deep ultraviolet photolithography. The SIS junctions were patterned from the Nb/AlN/NbN trilayer by successive RIE of the NbN layer using CF₄, by RF sputtering of AlN/Al film in Ar plasma and, finally, by RIE of the Nb layer using CF₄. The dielectric layer for junction insulation consists of 250 nm SiO₂, defined in a self-aligned lift-off procedure. In the final step, a 500 nm thick top microstrip electrode made of Al was deposited via DC magnetron sputtering. Afterwards, the thickness of the quartz substrate was reduced to 40 μm by mechanical polishing.

The Nb/AlN/NbN junctions fabricated onto an Si substrate with a 200 nm Nb layer and a 100 nm NbN film have a gap voltage $V_g = 3.7$ mV and a quality factor (the ratio of the subgap to the normal state resistance) $R_j/R_n > 30$ for $R_n A$ approximately 30 Ω · μm², while showing $V_g = 3.4$ mV and $R_j/R_n = 23$ for the higher current density ($R_n A = 7$ Ω · μm²) and the submicrometer (0.5 μm²) junction area. In contrast, the current SIS junctions with considerably thinner Nb electrodes (100 nm) and which were fabricated onto the NbTiN film have $V_g = 3.2$ mV for $R_n A = 7$ Ω · μm² (see Fig. 7.13). We cannot completely explain yet the cause of such a decrease of the junction gap voltage.

7.1.3 NbN Tunnel Junctions with MgO Barrier

For many years, tunnel junctions based on niobium nitride (NbN) have been attracting interest as an alternative to Nb junctions for high-frequency applications because NbN has a large gap energy. There have been many reports on the development of NbN tunnel junctions using different tunnel barrier materials [47–50]. Initially, only NbN/MgO/NbN junctions exhibited reasonably good quality,

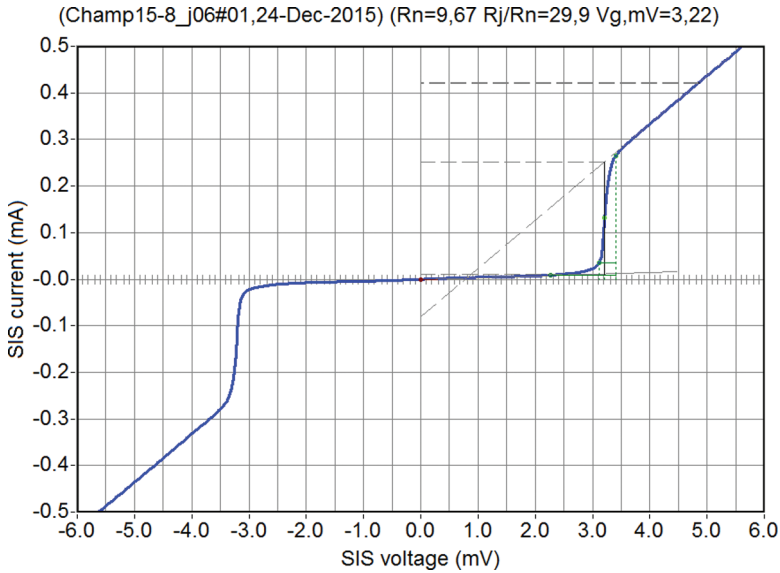


Figure 7.13 IVC of the twin Nb–AlN–NbN mixer element fabricated onto a SiO_2 substrate for APEX (area of each tunnel junction $S = 0.37 \mu\text{m}^2$, $V_g = 3.22 \text{ mV}$, $R_n S = 7 \Omega \cdot \mu\text{m}^2$, J_g of approximately 34 kA/cm^2). The Josephson supercurrent is suppressed by the magnetic field.

because both NbN and MgO have the same crystal structure with a lattice mismatch of less than 5%. Recently, high-quality epitaxial NbN/AlN/NbN tunnel junctions with a wide range of current densities have been demonstrated [51–54]. Although previous works have proven the possibility of producing high-quality, all-NbN tunnel junctions, we have developed a new technique to fabricate NbN/MgO/NbN circuits. Our approach [17] resembles the “classical” technique proposed many years ago for the production of Nb/AlO_x/Nb junctions [23], which are the basic building blocks for most devices of modern superconducting electronics. According to our approach, a very thin Mg layer (approximately only 1.5 nm) is DC-sputtered on the NbN layer, and the Mg is then oxidized in the O₂ plasma (this is similar to the Al nitridization process used for the fabrication of Nb/AlN/NbN junctions [39, 55]).

The transmission electron microscopy (TEM) image (Fig. 7.14) shows the layered structure of the junction area of the sample. The

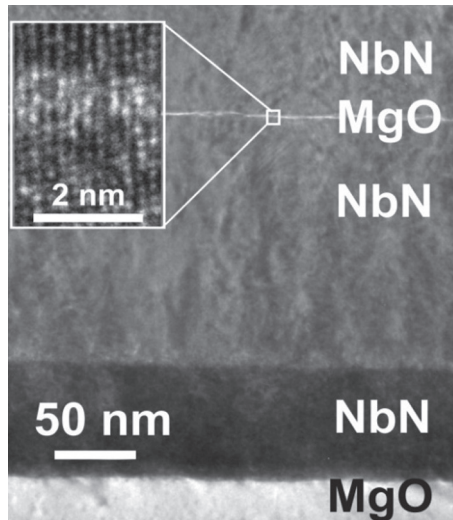


Figure 7.14 The transmission electron microscopy image of the layered NbN/MgO/NbN structure. Reproduced with permission from Koshelets et al. [17].

MgO substrate, the bottom and top NbN electrodes, and the MgO barrier are visible. The bottom electrode consists of the epitaxial 70 nm NbN monitor layer covered by a 150 nm thick NbN film, which is polycrystalline due to the lift-off structuring of this and all subsequent layers. The top NbN electrode is polycrystalline and has a thickness of 70 nm. A high-resolution TEM image of the 1.5 nm thick MgO barrier layer is shown in the insert of the picture. It was observed that the orientation of the crystal structure of NbN electrodes is maintained across the MgO barrier.

By using the developed technique, it is possible to fabricate high-quality junctions with a quasiparticle tunnel current density J_g in the range of 0.05–80 kA/cm². The IVC of the NbN/MgO/NbN junction ($J_g = 2$ kA/cm²) is shown in Fig. 7.15; the dependencies of the gap voltage V_g and the quality factor R_j/R_n (the ratio of the leakage resistance R_j and the normal state resistance R_n) on the current density are presented in Fig. 7.16. To summarize, a new technique for fabrication of high-quality SIS tunnel junctions based on epitaxial NbN films with an MgO barrier has been developed;

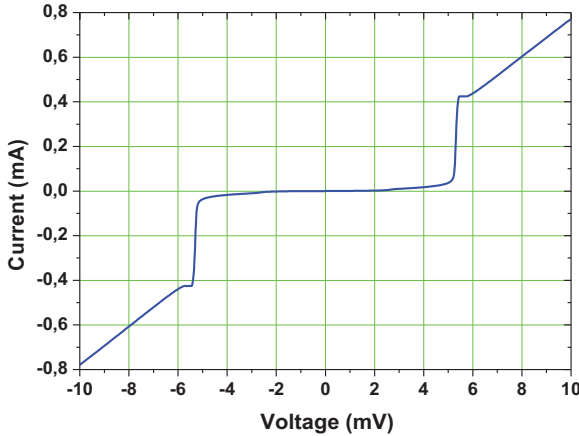


Figure 7.15 IVC of the NbN/MgO/NbN junction (I_c is suppressed by the magnetic field): $S = 18 \mu\text{m}^2$, $J_g = 2 \text{ kA/cm}^2$, $V_g = 5.3 \text{ mV}$, $R_n = 11.7 \Omega$, $R_j(2 \text{ mV})/R_n = 80$, $R_j(4 \text{ mV})/R_n = 19.5$. Reproduced with permission from Koshelets et al. [17].

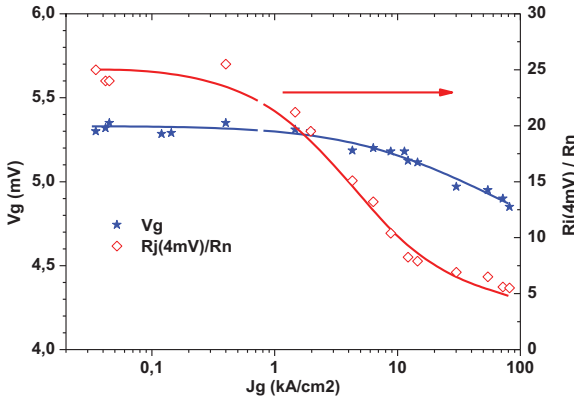


Figure 7.16 Dependencies of the NbN/MgO/NbN junction's parameters on the current density J_g . Experimental points are connected by lines as a guide for the eye. Reproduced with permission from Koshelets et al. [17].

junctions with a gap voltage $V_g = 5.3 \text{ mV}$ and a quality barrier parameter $R_j(4 \text{ mV})/R_n > 25$ have been fabricated. Such junction parameters are very promising for the development of an SIR for frequencies well above 1 THz.

7.2 Superconducting Terahertz Oscillators

Josephson junctions have been considered as natural terahertz oscillators for more than half a century, ever since Josephson discovered the effects named after him [56, 57]. Since that time, many quite different types of Josephson oscillators have been proposed and studied [58–68], but only a few of them were developed at level suitable for real applications. Let us consider one of the most attractive applications: the direct integration of a Josephson local oscillator (JLO) with the most sensitive heterodyne SIS mixer. There are a number of important requirements of the JLO's properties to make it suitable for application in the phase-locked superconducting integrated receiver (SIR). The continuous frequency tuning of the JLO over a wide frequency range (usually more than 100 GHz) and a possibility of the JLO's phase stabilization at any frequency in the operation range are required for most applications. The output power of the JLO should be sufficient to pump the matched SIS mixer within a wide frequency range and it can be electronically adjusted. Obviously, the JLO should emit enough power to pump an SIS mixer (of about 1 μW), taking into account a specially designed mismatch of about 5–7 dB between the JLO and the SIS mixer, which was introduced to avoid leakage of the input signal to the LO path. It is a challenge to realize the ultimate performance of the separate superconducting elements after their integration into a single-chip device. Another very important issue is the linewidth of the JLO. Even for wideband room-temperature PLL systems, the effective regulation bandwidth is limited by the length of the cables in the loop (about 10 MHz for a typical loop length of two meters). This means that the free-running JLO linewidth has to be well below 10 MHz to ensure stable JLO phase locking with a reasonably good spectral ratio (SR)—the ratio between the carrier and the total power emitted by the FFO [75].

7.2.1 Nb-Based Flux-Flow Oscillators

The Josephson flux flow oscillators (FFOs) [69–74] based on Nb–AlO_x–Nb and Nb–AlN–NbN junctions have proven [15, 16, 75] to be the most developed superconducting local oscillator for

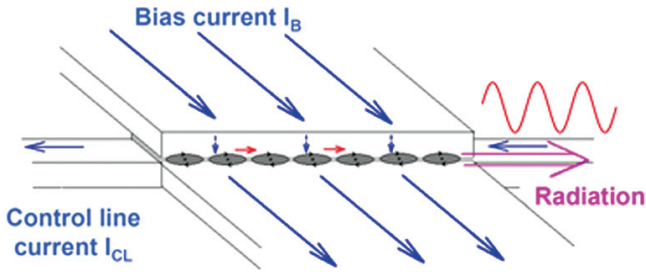


Figure 7.17 Schematic view of a flux-flow oscillator [16].

integration with an SIS mixer in a single-chip submicrometer-wave superconducting integrated receiver [14–21]. The FFO is a long Josephson tunnel junction of the overlapped geometry (see Fig. 7.17) in which an applied DC magnetic field and a DC bias current, I_B , drive a unidirectional flow of fluxons, each containing one magnetic flux quantum, $\Phi_0 = h/2e \approx 2 \cdot 10^{-15}$ Wb. Symbol h represents Planck's constant and e is the elementary charge. An integrated control line with the current I_{CL} is used to generate the DC magnetic field that is applied to the FFO. According to the Josephson relation, the junction oscillates with a frequency $f = (1/\Phi_0) \cdot V$ (about 483.6 GHz/mV) if it is biased at voltage V . The fluxons repel each other and form a chain that moves along the junction. The velocity and density of the fluxon chain, and thus the power and frequency of the submicrometer-wave signal emitted from the exit end of the junction due to the collision with the boundary, may be adjusted independently by the appropriate settings of I_B and I_{CL} . The FFO differs from the other members of the Josephson oscillator family by the need for these two control currents, which in turn provides the possibility of an independent frequency and power tuning.

We experimentally investigated [16, 75] a large number of the FFO designs. The length, L , and the width, W , of the FFO used in our study were 300–400 μm and 4–48 μm , respectively. The value of the critical current density, J_C , was in the range of 4–8 kA/cm^2 , giving a Josephson penetration depth of $\lambda_J \approx 6$ –4 μm . The corresponding value of the specific resistance was $R_n^* L^* W$ is ~ 50 –25 $\Omega^* \mu\text{m}^2$. For the numerical calculations we used a typical value of the London

penetration depth, $\lambda_L \approx 90$ nm, for all-Nb junctions, and a junction-specific capacitance $C_s \approx 0.08$ pF/ μm^2 . The active area of the FFO (i.e., the AlO_x or the AlN tunnel barrier) is usually formed as a long window in the relatively thick (200–250 nm) SiO_2 insulation layer, sandwiched between the two superconducting films (the base and wiring electrodes). The so-called idle region consists of the thick SiO_2 layer adjacent to the junction (on both sides of the tunnel region) between the overlapping electrodes. It forms a transmission line parallel to the FFO (not shown in Fig. 7.17). The width of the idle region ($W_1 = 2\text{--}14$ μm) is comparable to the junction width. The idle region must be taken into account when designing an FFO with the desired properties. In our design, it is practical to use the flat-bottomed electrode of the FFO as a control line in which the current I_{CL} produces the magnetic field, which is mainly applied perpendicular to the long side of the junction.

Previously, the Nb– AlO_x –Nb or Nb– AlN –Nb trilayers were successfully used for the FFO's fabrication. Traditional all-Nb circuits are constantly being optimized but there seems to be a limit for linewidth optimizations at certain boundary frequencies due to the Josephson self-coupling (JSC) effect [76], as well as a high frequency limit, imposed by the Nb gap frequency (~ 700 GHz). This is the reason to develop novel types of junctions based on materials other than Nb. We reported on the development of the high-quality Nb– AlN –NbN junction-production technology [39]. The implementation of an AlN tunnel barrier in combination with an NbN top superconducting electrode provides a significant improvement in the quality of the SIS junction. The gap voltage of the junction $V_g = 3.7$ mV. From this value, and the gap voltage of the Nb film $\Delta_{\text{Nb}}/e = 1.4$ mV, we have estimated the gap voltage of our NbN film as $\Delta_{\text{NbN}}/e = 2.3$ mV [40]. The use of Nb for the top “wiring” layer is preferable due to smaller losses of Nb when compared to NbN below 720 GHz. Furthermore, the matching structures developed for the all-Nb SIRs can be used directly for the fabrication of receivers with Nb– AlN –NbN junctions. The general behavior of the new devices is similar to that of the all-Nb ones; even the control currents, necessary to provide magnetic bias for the FFO, were nearly the same for the FFOs of similar designs.

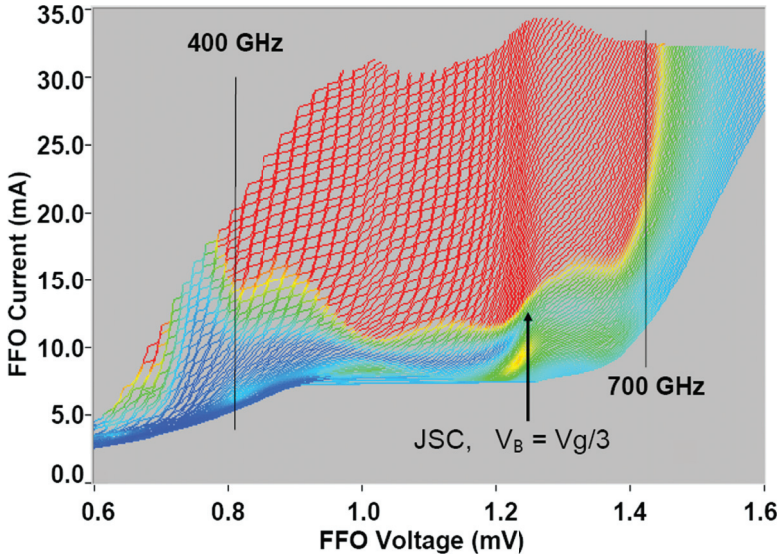


Figure 7.18 IVCs of the Nb–AlN–NbN FFO, measured at different magnetic fields produced by the integrated control line. The color scale shows the level of the DC current’s rise at the HM induced by the FFO. The red area marks the region of the FFO’s parameters where the HM current induced by the FFO exceeds 25% of the I_g . This level is well above the optimal value for an SIS-mixer operation [16].

A family of the Nb–AlN–NbN FFO IVCs, measured at different magnetic fields produced by the integrated control line, is presented in Fig. 7.18 ($L = 300 \mu\text{m}$, $W = 14 \mu\text{m}$, $W_1 = 10 \mu\text{m}$). A single SIS junction with an inductive tuning circuit was employed as a harmonic mixer (HM) for the linewidth measurements. The tuning and matching circuits were designed to provide “uniform” coupling in the frequency range of 400–700 GHz. Measured values of the HM current induced by the FFO oscillations (HM pumping) are shown in Fig. 7.18 by the color scale. The HM pumping for each FFO bias point was measured at a constant HM bias voltage of 3 mV (pumping is normalized on the current jump at the gap voltage, $I_g = 140 \mu\text{A}$). From Fig. 7.18, one can see that an FFO can provide a large enough power over the wide frequency range, which is limited at higher frequencies only by the Nb superconducting gap in transmission line

electrodes (base and wiring layers) and below 400 GHz by the design of the matching circuits.

The feature at approximately 600 GHz where the curves get denser is a JSC (Josephson self-coupling) boundary voltage. It was initially observed for all-Nb FFOs [76]. The JSC effect is the absorption of the FFO-emitted radiation by the quasi-particles in the cavity of the long junction. It considerably modifies the FFO's properties at the voltages $V \approx V_{\text{JSC}} = 1/3 * V_g$ (V_{JSC} corresponds to 620 GHz for the Nb-AlN-NbN FFO). Just above this voltage, the differential resistance increases considerably; that results in an FFO-linewidth broadening just above this point. This, in turn, makes it difficult or impossible to phase-lock the FFO in that region. For an Nb-AlO_x-Nb FFO, the transition corresponding to $V_{\text{JSC}} = V_g/3$ occurs around 450 GHz. Therefore, by using the Nb-AlN-NbN FFOs we can cover the frequency gap from 450 to 550 GHz that is imposed by the gap value of all-Nb junctions. The feature in Fig. 4 around 1 mV is very likely due to a singularity in the difference between the superconducting gaps $\Delta_{\text{NbN}} - \Delta_{\text{Nb}}$.

Continuous frequency tuning at frequencies below 600 GHz for the Nb-AlN-NbN FFOs of moderate length is possible, although the damping is not sufficient to completely suppress the Fiske resonant structure at frequencies below $V_g/3$. For short junctions with a small α (wave attenuation factor), the distance between the steps in this resonant regime can be as large, so that it is only possible to tune the FFO within a certain set of frequencies. For a 300–400 μm long Nb-AlN-NbN junction, this is not the case—the quality factor of the resonator formed by a long Nb-AlN-NbN Josephson junction is not so high at frequencies > 350 GHz. Therefore, the resonance steps are slanting and the distance between them is not so large (see Fig. 7.18). This allows us to set any voltage (and any frequency) below V_{JSC} , but for each voltage, only a certain set of currents should be used. Therefore, in this case, we have the regions of forbidden bias-current values, which are specific for each voltage below V_{JSC} , instead of the forbidden voltage regions for the Fiske regime in Nb-AlO_x-Nb FFO [40]. Special algorithms have been developed for automatic working-point selection in flight.

The typical current–voltage characteristics (IVCs) of an Nb-AlN-NbN SIS junction of an area approximately $1 \mu\text{m}^2$ is given in Fig. 7.19,

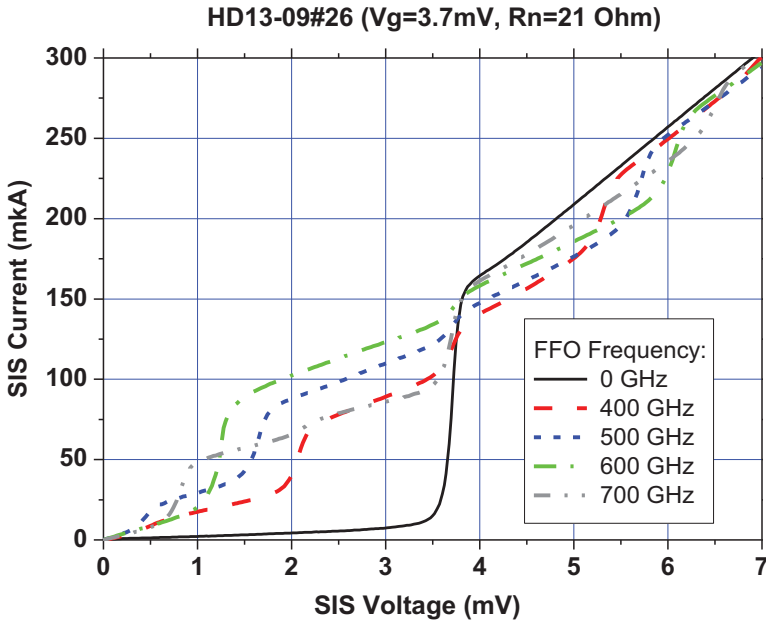


Figure 7.19 The IVCs of the SIS mixer: unpumped = solid curve; pumped at different frequencies = dashed and dotted lines (color online) [16].

which represents both the unpumped IVC (the solid line) and the IVC when pumped by an Nb–AlN–NbN FFO at different frequencies (dotted lines). One can see that the FFO provides more than enough power for the mixer pumping. In this experiment, we used the test circuits with low-loss matching circuits tuned between 400 and 700 GHz. Even with the specially introduced 5 dB FFO/SIS mismatch (required for the SIR operation), the FFO delivered enough power for the SIS mixer’s operation in the frequency range of 400–700 GHz. An important issue for the SIR’s operation is a possibility to tune the FFO’s power, while keeping the FFO frequency constant. This is demonstrated in Fig. 7.20, where the IVCs of an SIS mixer pumped at the FFO frequency of 500 GHz are shown, while they were being pumped at different FFO bias currents (different powers). Our measurements demonstrated [16, 75] that the FFO power can be adjusted in the range of 0–15 dB while keeping the same frequency, by proper adjustment of the FFO control line current.

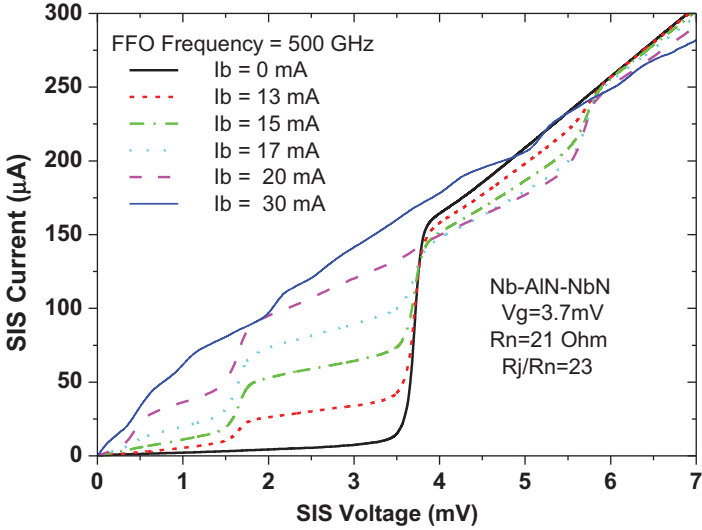


Figure 7.20 The IVCs of the SIS mixer: unpumped = black solid curve; pumped at different FFO bias currents (different powers) = lines with symbols; FFO frequency = 500 GHz (color online) [16].

7.2.2 Linewidth of the Flux-Flow Oscillator and Its Phase-Locking

The FFO linewidth (LW) has been measured in a wide frequency range from 300 GHz up to 750 GHz by using a specially developed experimental technique [77–80]. A specially designed integrated circuit incorporates the FFO junction, the SIS harmonic mixer and the microwave matching circuits (see Fig. 7.21). Both junctions are fabricated from the same Nb/AlN/NbN or Nb/AlO_x/Nb trilayer. A block diagram of the set-up for the linewidth measurements is shown in Fig. 7.22 [78]. The FFO signal is fed to the harmonic mixer (a SIS mixer operated in Josephson or quasiparticle mode) together with a 17–20 GHz reference signal from a stable synthesizer. The required power level depends on the parameters of the HM; it is about of 1 µW for a typical junction area of 1 µm². The intermediate frequency (IF) mixer product ($f_{IF} = \pm(f_{FFO} - n \cdot f_{SYN})$) at ~400 MHz is first boosted by a cooled HEMT amplifier ($T_n \approx 5$ K, gain = 30 dB) and then by a high-gain room-temperature amplifier.

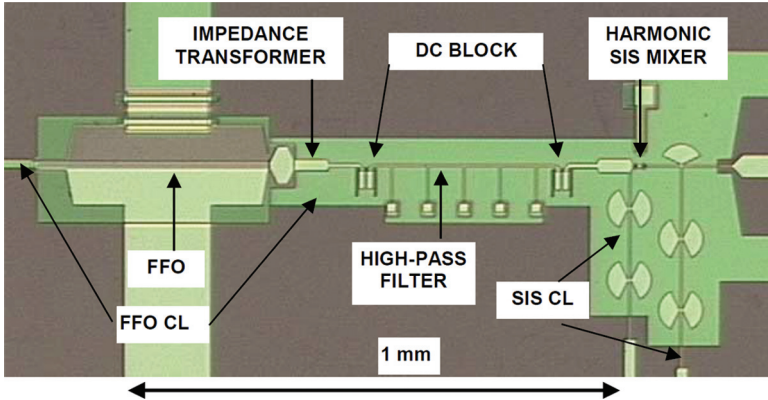


Figure 7.21 The central part of the microcircuits used for FFO linewidth measurements [79].

In order to accurately measure the FFO line shape, the IF signal must be time-averaged by the spectrum analyzer. To remove low-frequency drift and interference from the bias supplies, temperature drift, etc., we used a narrow band (<10 kHz) Frequency Discriminator (FD) system with a relatively low loop gain for the frequency locking of the FFO. With the FD narrow-band feedback system that stabilizes the mean frequency of the FFO (but which does not affect FFO's line shape), we can accurately measure the free-running FFO linewidth, which is determined by the much faster internal ("natural") fluctuations (see Fig. 7.23). The measured data are symmetrized relative to the center's frequency; these data are shown by diamonds. The profile of the FFO line recorded when biased at the steep Fiske step (FS), where the differential resistance is extremely small, can be different from the one measured on the smooth flux-flow step. Theoretically [58], the shape is Lorentzian for wideband fluctuations, while for narrow-band interference, at frequencies smaller than the autonomous FFO linewidth δf_{AUT} , the profile will be Gaussian; the theoretical curves are also shown in Fig. 7.23 for comparison. The theoretical lines providing the best fit near the peak are shown by the solid line and the dashed line for the Lorentzian and Gaussian profiles, respectively. The coincidence between the calculated curve and the symmetrized experimental

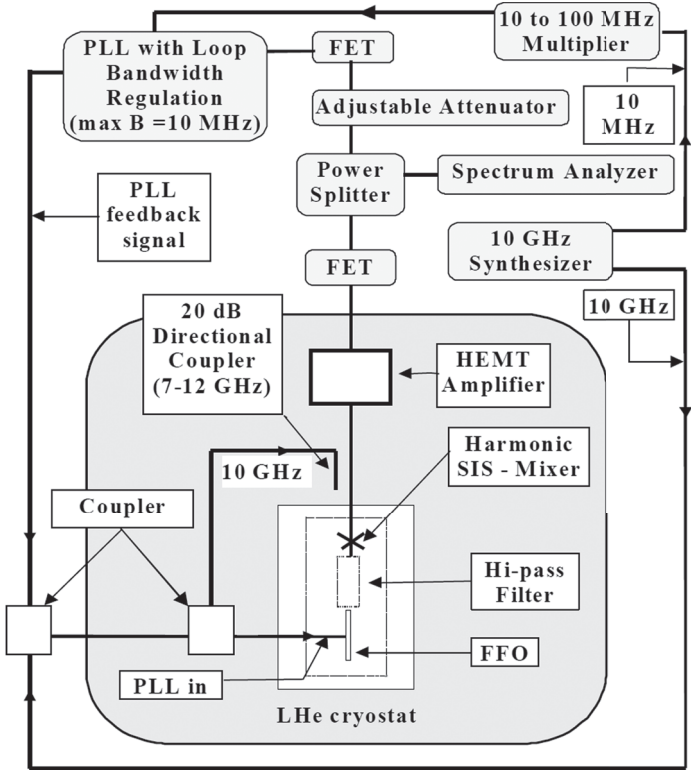


Figure 7.22 Block diagram of the PLL circuit and set-up for linewidth measurement. Reproduced with permission from Koshelets et al. [78].

data is excellent, and actually better than 5% in the emitted power, if a minor amplifier’s nonlinearity of about 0.4 dB is taken into account.

The resulting IF signal is also supplied to the phase-locking loop (PLL) system. The phase-difference signal of the PLL is fed to the FFO control-line current [15, 16, 75, 78–81]. Wideband operation of the PLL (10–15 MHz full width) is obtained by minimizing the cable loop’s length. A part of the IF signal is delivered to the spectrum analyzer via a power splitter (see Figs. 7.24 and 7.25). All instruments are synchronized to the harmonics of a common 10 MHz reference oscillator. Dependencies of the free-running FFO linewidth and the Spectral Ratio (SR) for the phase-locked FFO on

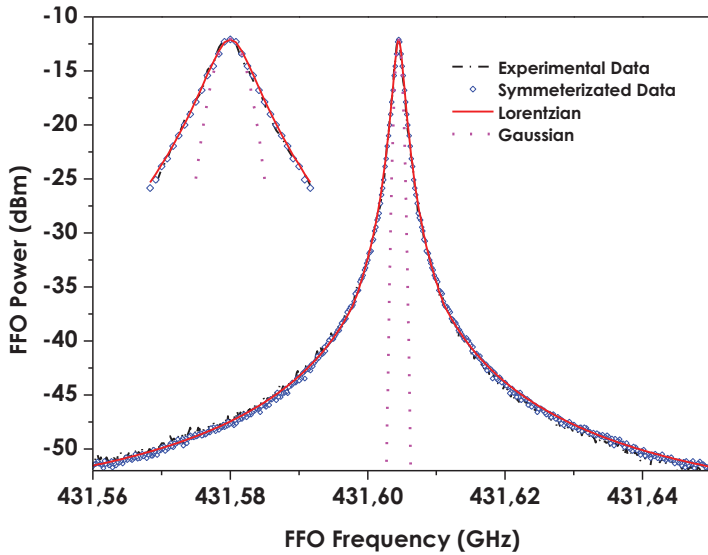


Figure 7.23 The FFO spectrum measured when biased on the Fiske step ($V_{\text{FFO}} = 893 \mu\text{V}$, $R_d = 0.0033 \Omega$, $R_d^{\text{CL}} = 0.00422 \Omega$, $\delta f_{\text{AUT}} = 1.2 \text{ MHz}$) is represented by the dash-dotted line. The symmetrized experimental data are shown by diamonds. The fitted theoretical Lorentzian and Gaussian profiles are shown by solid and dotted lines, respectively. The inset shows a close-up view of the central peak with the frequency axis multiplied five times [80].

frequency for two different FFO technologies (Nb- O_x -Nb and Nb-AlN-NbN) are presented in Fig. 7.26. One can see that $\text{SR} > 70\%$ can be realized for Nb-AlN-NbN FFO in the range of 250–750 GHz.

7.2.3 Sub-Terahertz Sound Excitation and Detection by Long Josephson Junctions

Interaction between phonons and electrons has attracted the attention of researchers over the years. Such interaction has been demonstrated by the use of an AC Josephson current for phonon generation in superconducting tunnel junctions [82, 83]; in these papers, a few possible mechanisms for phonon generation were considered. Direct generation of acoustic waves by the AC Josephson oscillations occurs when the tunnel barrier is piezoelectric. On the

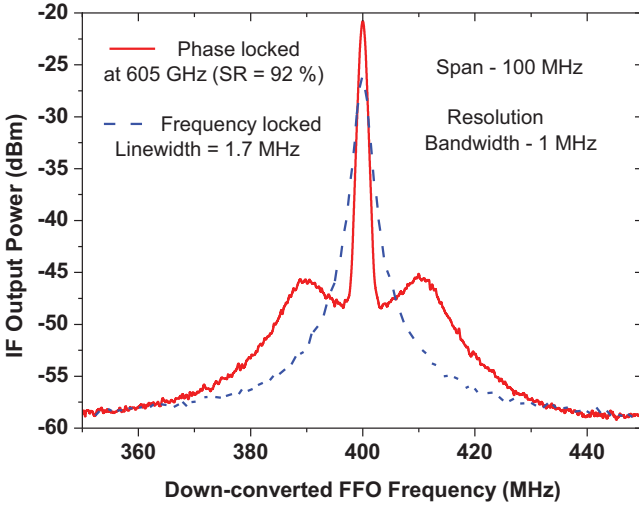


Figure 7.24 Spectra of the Nb-AlN-NbN FFO operating at 605 GHz (blue dashed line = frequency locked by FD; red solid line = phase-locked). Linewidth = 1.7 MHz; spectral ratio = 92% (color online).

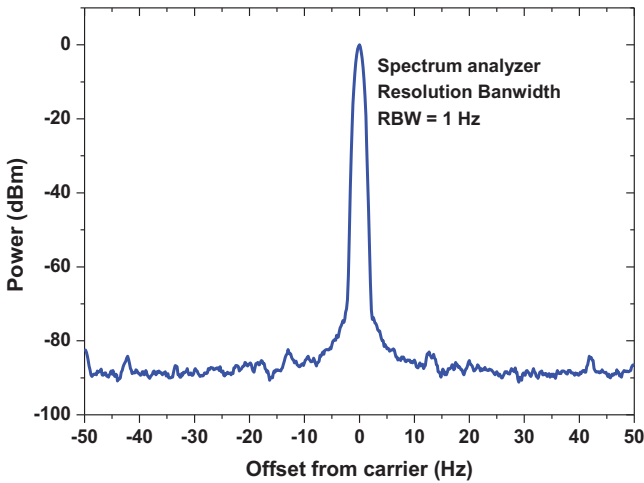


Figure 7.25 Spectra of the phase-locked Nb-AlN-NbN FFO operating at 605 GHz. Span = 100 Hz, RBW = 1 Hz, signal-to-noise ratio = 87 dB as measured in a bandwidth of 1 Hz.

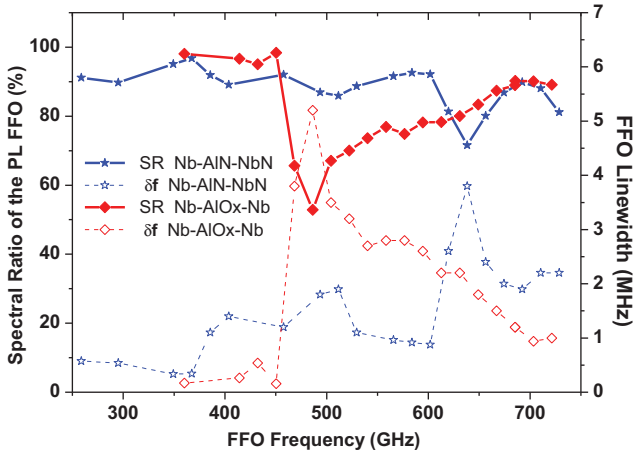


Figure 7.26 Dependencies of the free-running FFO linewidth and the spectral ratio for the phase-locked FFO on frequency. Data are presented for two different FFO technologies: Nb-O_x-Nb (represented by diamonds) and Nb-AlN-NbN (asterisks).

other hand, the need for an alternative explanation was suggested in reference [83] because the effect was observed in junctions with an amorphous barrier, and amorphous materials are typically not piezoelectric (although some materials may become piezoelectric in the amorphous state because amorphization can remove the inversion symmetry [84]). Therefore, it was suggested that, in the disordered material, the AC electrical field may instead act on uncompensated static charges with a finite dipole moment [83, 85, 86], resulting in the coherent generation of acoustic waves. The coupling strength of this process depends on the oxide properties; it can be comparable to (or even be well above the state of) Werthamer processes [87], which are basically the absorption of AC Josephson radiation energy by the quasiparticles and consequent photon-assisted tunneling—the so-called effect of Josephson self-coupling (JSC) [76, 87, 88].

The reverse effect—phonon-induced increase in the critical current of Josephson junctions [89] and appearance of the constant-voltage steps in the IVCs of the SNS junctions [90]—has been observed experimentally under low-frequency phonon excitation.

Interaction of the AC Josephson current and phonons was also found for intrinsic HT_c Josephson junctions [91–94]; it was observed as the occurrence of specific subgap structures in the form of current peaks (resonances) in the IVCs of these junctions. The obtained results have been explained [94–97] by the coupling between the intrinsic Josephson oscillations and phonons. Some time ago, a quite unusual superfine resonance structure (SFRS) was observed [98] in the IVCs of the Nb– AlO_x –Nb flux-flow oscillator (FFO); at that time, no reasonable explanation was proposed.

For comprehensive analysis of the superfine resonance structure [99], we have studied Nb– AlO_x –Nb and Nb–AlN–NbN FFOs. The length, L , and the width, W , of the tunnel junctions used in our study are 400 μm and 16 μm , respectively. The value of the critical current density, J_c , is in the range of 4–8 kA/cm^2 —giving a Josephson penetration depth of $\lambda_J = 6\text{--}4 \mu\text{m}$. The active area of the FFO (i.e., the AlO_x or the AlN tunnel barrier) is formed as a long window in the relatively thick (200 nm) SiO_2 insulation layer that is sandwiched between two superconducting films (base and wiring electrodes). The FFOs were fabricated from a high-quality trilayer structure [39] on the monocrystalline silicon substrate of (001) orientation. We used commercially available double-side polished silicon wafers (room temperature resistivity $> 10 \text{ k}\Omega\cdot\text{cm}$, thickness $d_S = 0.3 \pm 0.01 \text{ mm}$).

For wideband measurements of the FFO spectra, a superconductor–insulator–superconductor (SIS) mixer has been integrated on the same chip with the FFO [77]—see the previous section; a simplified sketch of the device under the test is presented in the inset to Fig. 7.27a. The FFO and the SIS junction are connected by a specially designed microstrip circuit that provides RF coupling in the range of 300–800 GHz, while the break at DC gives us a possibility to bias and measure both devices independently; this circuit is presented schematically in the inset to Fig. 7.27a by a dashed line and the capacitor. Due to the strong nonlinearity of the SIS mixer, it was utilized as a high-number harmonic mixer (HM) [30], in which the FFO signal under investigation beats with the n -th harmonic of an applied reference signal (of about 20 GHz), which was fed to the SIS mixer via a coaxial cable from a synthesized signal generator. Signals at down-converted frequencies $f_{IF} = f_{FFO} - n \cdot f_{ref}$

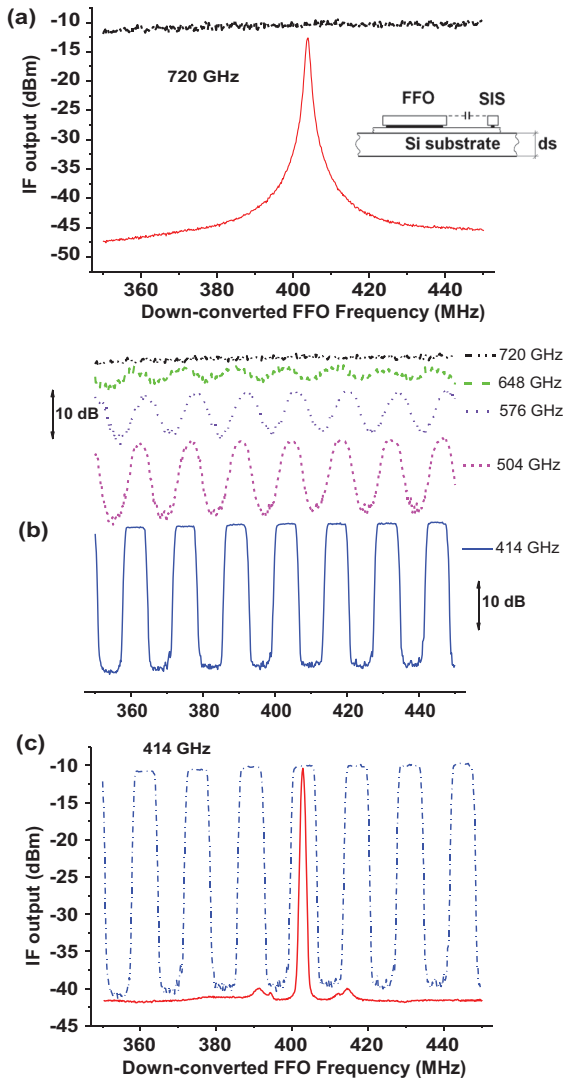


Figure 7.27 (Color online) [99]. Down-converted spectra of the Nb-AlO_x-Nb FFO measured at different FFO frequencies at $T = 4.2$ K by a spectrum analyzer in the regime “Max Hold” (see text) with resolution band width (RBW) = 1 MHz at fine tuning of the bias current; the frequency-locked FFO spectra measured at the FFO frequencies 720 and 414 GHz are presented by solid lines in graphs “a” and “c.” A sketch of the experimental sample is shown as an inset to Fig. 7.27a (see text).

can be analyzed using a conventional spectrum analyzer. The down-converted signals measured at the FFO frequencies ranging from 414 to 720 GHz are presented in Fig. 7.27.

The spectrum of the frequency-locked FFO [77] operating at 720 GHz is shown in Fig. 7.1a by the solid line. The spectrum recorded at fine FFO frequency tuning in the range of 100 MHz is presented by the dash-dotted line. This spectrum was measured by using the so-called “Max Hold” regime, when the maximum value in each spectral channel of the analyzer (601 points per range) is memorized over a long enough period, providing that the FFO frequency is tuned by fine adjustment of the bias or CL current. The amplitude of the down-converted signal is almost constant for the FFO frequency 720 GHz (the dash-dotted line in Fig. 7.27a), while for the decreasing of the FFO frequency, a well-defined resonant structure appeared in the down-converted spectra (Fig. 7.1b).

At low FFO frequencies, the SFRS is very pronounced and the down-converted power in the dips is at least 1000 times (30 dB) smaller than in the case of the maximum level (see Fig. 7.1c); actually, the minimum level in this case is determined by the noise level of the HM. One can see that the FFO frequency can be continuously tuned only within a small range, while frequencies between these stable regions cannot be obtained. Even a small change of the bias current near the edge of the stable region results in a “jump” of the FFO voltage (frequency) to the next stable region. The distance between resonances is equal to 14.1 MHz; exactly the same resonance spacing was measured for all FFO frequencies and for all tested FFOs fabricated on the 0.3 mm-thick silicon substrates described above. Very similar behavior was also measured for the Nb–AlN–NbN junctions.

We attribute this superfine structure to the manifestation of resonant interaction of the acoustic waves with the Josephson oscillator. A few different mechanisms were proposed that may couple electron oscillations and phonons: (i) excitation of phonons in a tunnel barrier due to the electromagnetic interaction between the ionic charges and the charges of conduction electrons [82, 83, 85, 86, 93, 96, 97], or via the ac-Josephson effect in a tunnel barrier made from a piezo and ferroelectric materials; (ii) emission of phonons via non-equilibrium quasiparticle relaxation in the

electrodes (not the barrier) caused by electron–phonon interaction [94, 100–102] and (iii) the dependence of the tunneling-matrix element on lattice displacements [31, 95]. The mechanism for the generation of phonons in Josephson junctions [103] is based on the excitation of the long wavelength acoustic resonance modes in the dielectric layer of the contact, which can influence the shape of the IVC of the junction in the same way as the excitation of electromagnetic cavity modes. This approach was extended [95] by including in consideration *all* optical phonons in superconductors (not only in the intermediate dielectric layer). To distinguish between these mechanisms, additional research is required, but that is outside the scope of this chapter.

According to our explanation, the experimentally measured IVCs are caused by excitation of the standing acoustic waves in the Si substrate. It is known that a considerable part of the power emitted by the FFO is reflected back; at low damping, these oscillations may reach the entry end of the FFO, raising the standing waves that manifest themselves as the Fiske steps. The standing electromagnetic waves of large amplitude (existing at least on the emitting end of the junction) excite acoustic waves. Note that even at higher voltages ($V > V_g/3$, V_g is the gap voltage of the FFO), where the Fiske steps could be suppressed [76] due to higher dumping caused by the JSC effect, the standing electromagnetic waves still exist at the emitting end of the junction and can excite acoustic waves of considerable amplitude.

Since flatness (parallelism) of the Si substrates is fairly good (thickness variation is well below 5 μm over 100 mm wafer size), the acoustic wave is reflected back to the point of emission with an accuracy much better than 0.1 μm . At frequencies where the Si substrate's thickness is equal to the integer number of acoustic wavelengths, the reflected wave will arrive in phase with electromagnetic oscillations, resulting in an increase of the current amplitude, while in between these resonances, the oscillations will be suppressed.

At least two experimental facts lead to such a conclusion. Firstly, the frequency distance between two adjacent resonances coincides with the distance between sound resonances in the silicon substrate: $\Delta f = V_L/d_s^*2$, where V_L is the longitudinal speed of sound in Si along

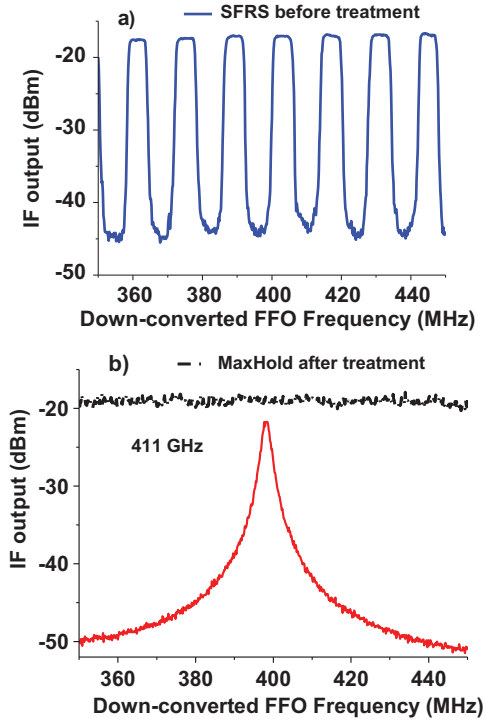


Figure 7.28 (Color online) [99]. Down-converted spectra of the Nb-AlO_x-Nb FFO fabricated on the 0.3 mm thick Si substrate before (a) and after abrasive treatment (b), measured at different FFO frequencies at $T = 4.2$ K using a spectrum analyzer in the “Max Hold” regime (see text). The frequency-locked FFO spectrum measured at the FFO frequency of 411 GHz is presented by solid lines in graph “b.”

the [001] direction. For $V_L = 8480$ m/s [104] and $d_s = 0.3$ mm, the calculated resonance spacing is 14.1 MHz, which corresponds precisely to experimentally measured data. The frequency distance between two adjacent resonances is inversely proportional to the substrate thickness d_s ; for the FFOs fabricated on a thicker Si substrate ($d_s = 0.525$ mm), the resonance spacing was about 8 MHz, which again corresponds well to the calculated value.

Secondly, after treatment of the opposite (bottom) substrate surface with an abrasive powder, the superfine resonant structure disappeared completely (see Fig. 7.28). We used a set of powders

with particle sizes from 1 to 10 μm , resulting in a root mean square (RMS) surface roughness that was measured by an atomic force microscope (AFM) to be 30–280 nm, which is well above the wavelength of the acoustic wave at 500 GHz of about 13 nm (note that for a polished Si surface, the RMS is approximately 0.1 nm; see, e.g., [105]). It seems that the acoustic waves that are reflected from a rough Si surface arrive at the FFO plane in an arbitrary phase. That fact makes the establishment of standing acoustic waves impossible, giving us the possibility to phase lock the FFO [81] at *any* desirable frequency, which is vitally important for most practical applications. It was found that chemical etching of the bottom surface of the Si substrate (RMS roughness of approximately 250 nm) also completely eliminates the appearance of the SFRS. Such Si substrates with a chemically etched bottom surface are commercially available and were used for the fabrication of an integrated receiver with a phased-locked FFO [39, 40], which was successfully implemented for atmosphere monitoring from a high-altitude balloon [15, 16, 20]. On the other hand, the roughness of the etched Si substrate is negligibly small at sub-THz frequencies, and allows good RF coupling of the integrated receiver that is installed on the flat surface of the synthesized elliptical Si lens [15, 16, 20].

This explanation of the SFRS was confirmed by a preliminary theoretical consideration [106], in which coherent phonon radiation and detection due to the interaction of Josephson's electromagnetic oscillations with a mechanical displacement field were analyzed. The Josephson tunneling structure together with a silicon substrate constitute a high overtone composite resonator for bulk acoustic waves that propagate normally to the layers. Resonant generation of coherent acoustic waves revealed itself as a superfine structure in IVC, similar to the usual Fiske steps that are caused by reflection of electromagnetic waves in the junction resonance cavity.

An ability of the Josephson junction to generate and to detect the coherent acoustic waves has been demonstrated experimentally at frequencies up to 800 GHz. Frequency resolution well below 1 MHz can be realized for the frequency (or phase-locked) FFO, and that opens new possibilities for solid-state physics research and phonon spectroscopy. The superfine resonant structure in the FFO IVCs is attributed to acoustic wave generation by the FFO and the excitation

of acoustic wave resonances in a thick Si substrate. The SFRS effect can be avoided by proper treatment of the bottom surface; on the other hand, this effect can be employed for high-resolution phonon spectroscopy at well-defined frequencies without additional FFO locking.

7.3 Superconducting Integrated Receivers

A superconducting integrated receiver (SIR) [14, 15] was proposed more than 10 years ago and has since then been developed up to the point of practical application [16–21]. Our approach [15, 16, 19] consists in developing a *single chip* heterodyne receiver, which is smaller and less complex than traditional devices. Typically, such a receiver consists of a number of main components (local oscillator, mixer, antenna structure, phase-lock circuit, etc.), which are usually built as separate units and are complex (and thus costly). According to our concept (see Fig. 7.29), we have integrated all these components into a single chip, reducing the overall system complexity in exchange for increased on-chip and lithographic fabrication complexity. An SIR comprises on a single chip all of the key elements needed for heterodyne detection: a low-noise SIS mixer with quasi-optical antenna, a flux-flow oscillator (FFO) [69–81] acting as a local oscillator (LO) and a second SIS harmonic mixer

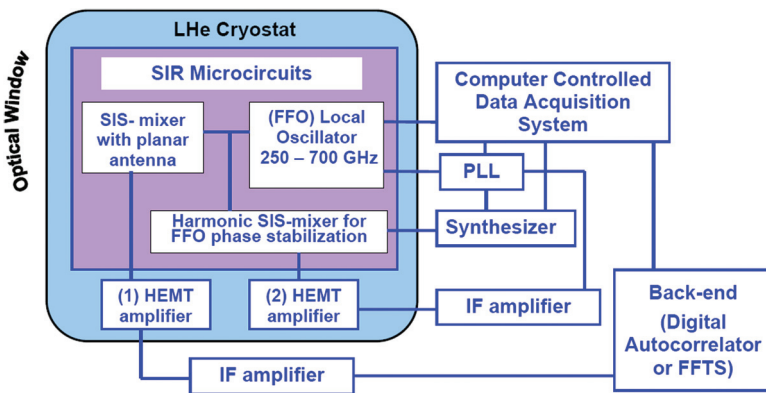


Figure 7.29 Block diagram of the superconducting integrated receiver.

(HM) for the FFO phase locking. The concept of the SIR looks very attractive for many practical applications due to its compactness and the wide tuning range of the FFO; a bandwidth up to 35% has been achieved with a twin-junction SIS mixer design. Recently, the frequency range of most practical heterodyne receivers was limited by the tunability of the local oscillator; nowadays, commercially available multipliers cover the band up to the 40% of the center's frequency [107], and the best SIS receivers (see, e.g., [108]) offer a bandwidth of 15–30%. Another potential advantage is the use of arrays of SIR channels within a single cryostat that could operate at the same or different LO frequencies.

One of the important practical applications of the SIR is TELIS (TErahertz and submillimeter Limb Sounder) [20, 109, 110]—a three-channel balloon-borne heterodyne spectrometer for atmospheric research that was developed in a collaboration between four institutes: Deutsches Zentrum für Luft- und Raumfahrt (DLR), Germany; Rutherford Appleton Laboratories (RAL), United Kingdom; and SRON—Netherlands Institute for Space Research, the Netherlands (in tight collaboration with Kotel'nikov Institute of Radio Engineering and Electronics, IREE, Moscow). All three receivers utilize state-of-the-art superconducting heterodyne technology and operate at 500 GHz (by RAL), at 480–650 GHz (by SRON + IREE) and at 1.8 THz (by DLR). TELIS is a compact, lightweight instrument capable of providing broad spectral coverage, high spectral resolution, and long flight duration. The TELIS instrument also serves as a test bed for many novel cryogenic technologies and as a pathfinder for satellite-based instrumentation.

TELIS is mounted on the same balloon platform (payload weight: 1200 kg) as the Fourier transform spectrometer MIPAS-B [111], developed by IMK (Institute of Meteorology and Climate Research of the University of Karlsruhe, Germany) and is operated in the mid-infrared range ($680\text{--}2400\text{ cm}^{-1}$). Both instruments observe the same air mass simultaneously, and together they yield an extensive set of stratospheric constituents that can be used for detailed analysis of atmospheric chemical models, such as ozone destruction cycles. In particular, the 480–650 GHz TELIS channel is able to measure vertical profiles of ClO, BrO, O₃, and its rare isotopologues, O₂, HCl, HOCl, H₂O, and its three rare isotopologues, HO₂, NO, N₂O,

NO_2 , HNO_3 , CH_3Cl , and HCN . In this paper, the design and technology of the 480–650 GHz channel as used in the flight configuration are presented in conjunction with the test results and the first preliminary scientific results.

7.3.1 The SIR Channel Design and Performance

A key element of the 480–650 GHz channel is the SIR [14–21] that comprises within a single chip (with a size of 4 mm*4 mm*0.5 mm, see Fig. 7.30) a low-noise SIS mixer with quasi-optical antenna, a superconducting FFO acting as an LO and a second SIS harmonic mixer (HM) for FFO phase-locking. To achieve the required instantaneous bandwidth of 480–650 GHz, a twin-SIS mixer with $0.8 \mu\text{m}^2$ junctions and a new design of the FFO/SIS matching circuitry were implemented. A microscope photograph of the central part of the SIR chip with a double-dipole antenna is presented in Fig. 7.31. All components of the SIR microcircuits were fabricated from a high-quality Nb-based trilayer on an Si substrate [14, 15].

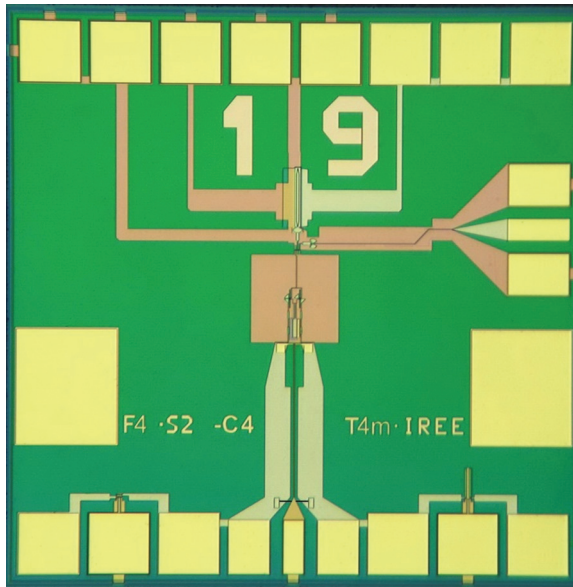


Figure 7.30 Photo of the SIR microcircuit with a double-slot antenna [16].

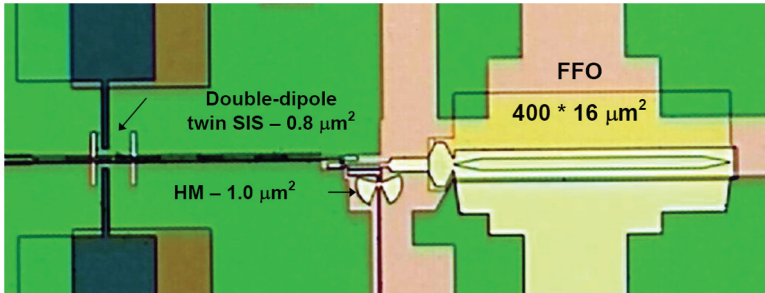


Figure 7.31 Central part of the SIR chip with a double-dipole antenna, a twin SIS-mixer, and a harmonic mixer for FFO phase locking [16].

The receiver chip was placed on the flat back surface of the elliptical silicon lens (forming an integrated lens-antenna) with accuracy of $10\ \mu\text{m}$, determined by the tolerance analysis of the optical system. As the FFO is very sensitive to external electromagnetic interferences, the SIR chip was shielded by two concentric cylinders: the outer cylinder was made from cryoperm and the inner one from copper with a $100\ \mu\text{m}$ coating of superconducting lead. All SIR channel components (including input optical elements) were mounted onto a single plate inside a $240\ \text{mm} \times 180\ \text{mm} \times 80\ \text{mm}$ box, which was cooled by the thermo-straps to a temperature of approximately $4.2\ \text{K}$.

The resolution of the TELIS back-end spectrometer is $2.160\ \text{MHz}$, sufficient to resolve the exact shape of atmospheric lines. The FFO line shape and spectral stability should ideally be much better than this. However, the free-running linewidth of the FFO can be up to $10\ \text{MHz}$; therefore, a phase-lock loop (PLL) has been developed to phase lock the FFO to an external reference oscillator [75–80]. For this, a small fraction of the FFO power was first directed to a so-called harmonic mixer (HM) placed on the SIR chip. The HM was pumped by an off-chip local oscillator source unit (LSU), which has a tunable reference frequency in the range of $19\text{--}21\ \text{GHz}$. The frequency of the LSU was chosen such that the difference frequency of the n th harmonic of the LSU, generated by the HM and the FFO, was about $4\ \text{GHz}$. This difference signal was then amplified by a cryogenic low-noise HEMT amplifier and down-converted to $400\ \text{MHz}$ by using a second reference at $3.6\ \text{GHz}$. Finally, the

frequency and phase of this 400 MHz signal was compared to yet another reference frequency of 400 MHz, and the resulting error signal was fed back to the FFO. The LSU and the reference signals at 3.6 GHz and at 400 MHz were all phase-locked to an internal, ultra-stable 10 MHz Master Oscillator.

The TELIS-SIR channel has been characterized in eight microwindows that have been selected for the flight in (Sweden). These microwindows have the following LO frequencies:

- 495.04 GHz for H₂¹⁸O
- 496.88 GHz for HDO
- 505.60 GHz for BrO
- 507.27 GHz for ClO
- 515.25 GHz for O₂, pointing, and temperature
- 519.25 GHz for BrO and NO₂
- 607.70 GHz for ozone isotopes
- 619.10 GHz for HCl, ClO, and HOCl

Initial flight values for the parameters for the FFO, SIS, and HM mixers have been determined for each microwindow. Dedicated algorithms allowing for fast switching between LO frequencies and for in-flight optimization of the SIR have been developed. It takes approximately 1 minute of stabilization and optimization to switch between two LO settings. All experimental results presented here have been obtained using the SIR flight device. After optimization of the FFO design, the free-running linewidth between 7 and 0.5 MHz was measured in the frequency range of 350–750 GHz, which allows the phase-locking of 35–95% of the emitted FFO. Examples of the free-running (frequency-locked) and the phase-locked spectra of the FFO, measured for the flight SIR at the FFO frequency 605 GHz, are presented in Fig. 7.24.

The measured double sideband (DSB) receiver's noise temperature T_R , uncorrected for any loss, is presented in Fig. 7.32 as a function of LO frequency. As can be seen, the noise is well below 200 K at all frequencies of interest, with a minimum of 120 K at 500 and 600 GHz. The noise peak around 540–575 GHz is partially spurious, caused by the absorption of water vapor in the path between the calibration sources and the cryostat,

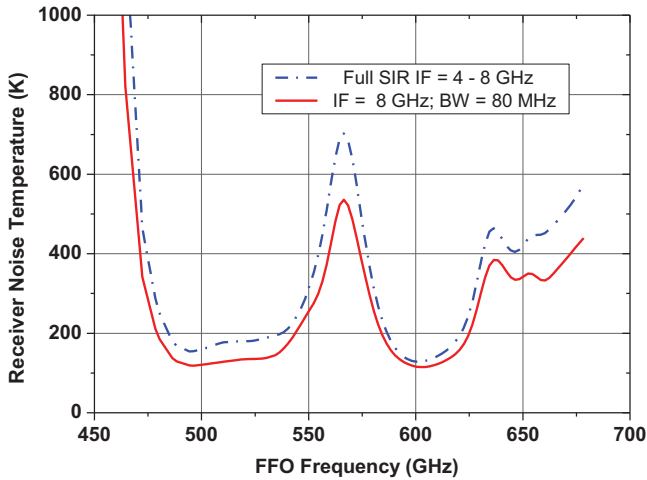


Figure 7.32 Measured DSB receiver noise temperature of the SIR device selected for flight at an 8 GHz IF frequency (red solid line) and integrated into the 4–8 GHz IF range (blue dashed line)—color online [16].

and partially real—due to the properties of the SIS-mixer tuning circuitry. The relatively high noise in this band is of no concern for scientific observations, since this part of the atmospheric spectrum is obscured by a highly saturated water-vapor line, rendering it virtually useless for atmospheric science. The noise as a function of IF is fairly flat in the frequency range of 4–8 GHz, as can be seen in Fig. 7.33, where the (DSB) receiver noise temperature is plotted as a function of IF frequency. The dependence of the receiver noise temperature on the SIS bias voltage is shown in Fig. 7.34 for the modified IF system; one can see that for Nb–AlN/NbN circuits there is very wide range of SIS bias voltages where T_R is almost constant.

The TELIS instrument had four successful flights: three in Kiruna, Sweden (2009, 2010, and 2011) and one in Timmins, Canada (2014); see Fig. 7.35. During all those flights, the shortest of which lasted 10 hours on float, thousands of limb spectra were measured. Examples of recently elaborated spectra measured by the SIR-TELIS channel at different LO frequencies are presented in Figs. 7.36 and 7.37 [17].

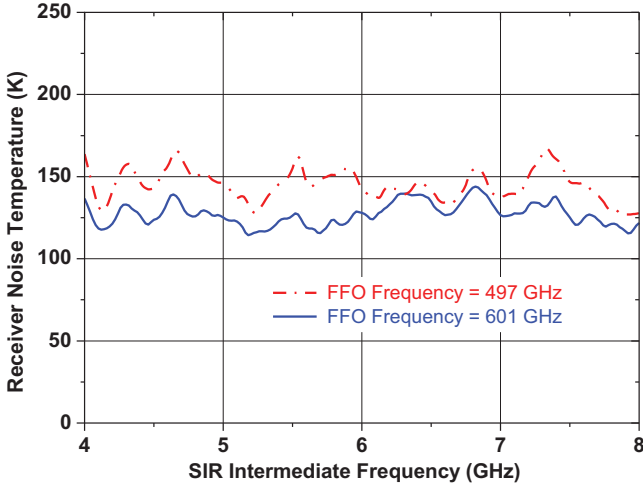


Figure 7.33 DSB receiver noise temperature as a function of the IF frequency, taken at two FFO frequencies: 497 and 601 GHz (color online) [16].

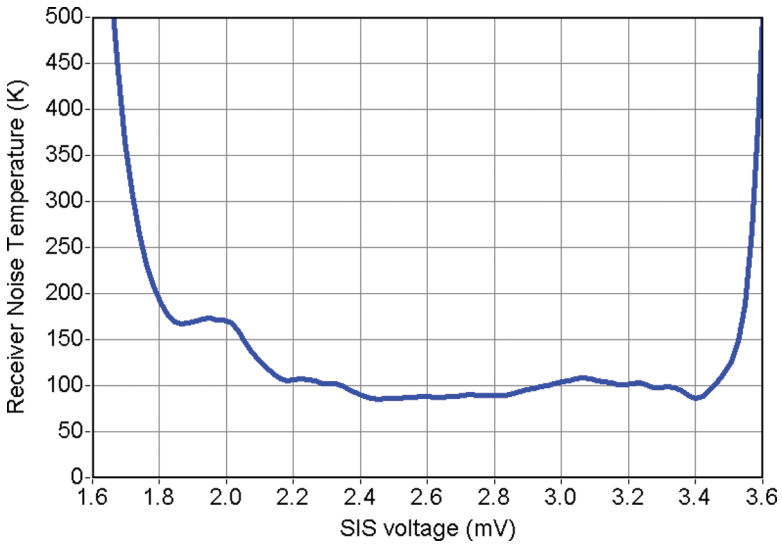


Figure 7.34 Receiver noise temperature as a function of the SIS bias voltage measured at the LO frequency 507 GHz in the full 4–8 GHz IF range [21].



Figure 7.35 TELIS-MIPAS launch at Esrange, Sweden; March 2009. Balloon size: $400,000 \text{ m}^3$.

The flights in northern Sweden focused on catalytic-ozone loss by halogens in the Arctic region, which is similar to processes causing the infamous ozone hole over the Antarctic. The spectra depicted in Figs. 7.36 and 7.37 [17] cover some core molecules to address these processes: namely, ozone itself and the Cl-bearing species HCl and ClO. ClO is the main form of active chlorine that is causing the catalytic destruction of ozone. HCl, on the other hand, is a so-called reservoir species as it is mostly inert in ozone chemistry. The ozone's destruction depends on the ClO concentration, which strongly depends on altitude. Limb sounding provides a tool to gain insight into the vertical distribution of these concentrations. A single recording of a spectrum mostly contains information on molecules at a tangent point, which is the lowest point in the atmosphere of the light path. By combining several spectra recorded at different tangent heights, a vertical profile can be constructed. The integration time of a single spectrum is 1.5 seconds and a typical limb scan typically contains 10–20 different recordings, covering tangent heights between 10 and 35 km, for a total measurement time, including calibration measurements, close to one minute. In the figures, only a few spectra from a given limb scan are shown to prevent cluttering.

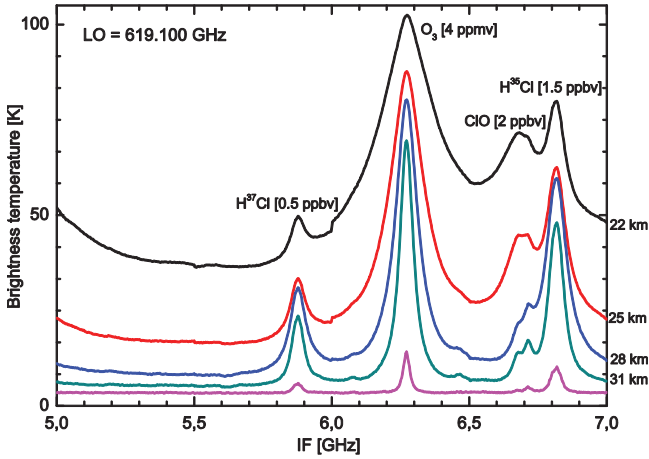


Figure 7.36 Spectra of two HCl isotopes, ozone and ClO. The LO frequency is 619.1 GHz. Spectra for tangent heights 22–31 km and upward looking 6° measured in Kiruna, 2010, are presented in the graph. Corresponding estimated concentrations of observed gases are shown. Reproduced with permission from Koshelets et al. [17].

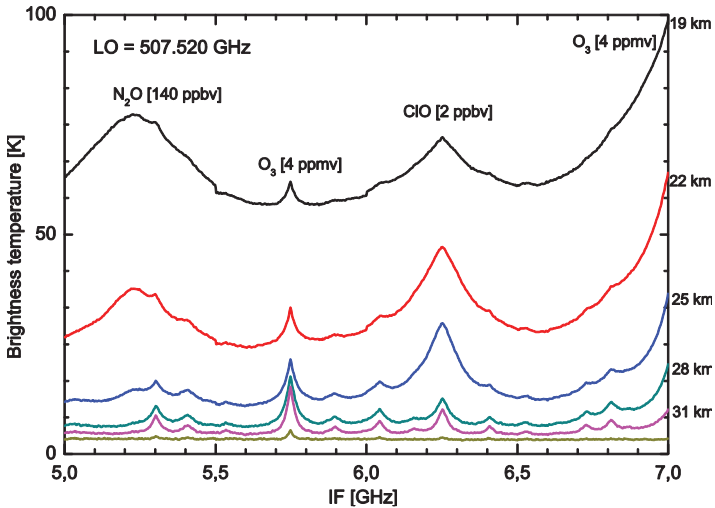


Figure 7.37 Spectra of ClO, ozone, and N_2O . The LO frequency is 507.52 GHz. Spectra for tangent heights 19–31 km and up-looking 6° measured in Kiruna, 2010, are presented in the graph. Reproduced with permission from Koshelets et al. [17].

For the results presented in Figs. 7.36 and 7.37 [17], limb scans' data were averaged 10 and 23 times, respectively. This calculation gives the total averaging time for one tangent height: about 16 seconds (in Fig. 7.36) and 35 seconds (in Fig. 7.37). To provide the same signal-to-noise ratio for the semiconductor-based receivers, which have noise temperatures not lower than 1800 K [112] in the same frequency range, the measurement time should be increased by two orders of magnitude, at least. The wideband coverage of the FFO gives the advantage that a huge number of molecules, whose absorption lines lie in the FFO-tuning range, can be measured during one campaign. The TELIS-SIR channel has been characterized in eight microwindows covering the FFO frequency range from 495.04 GHz (for H_2^{18}O) to 619.10 GHz (for HCl, ClO, and HOCl); in combination with a short integration time, this gives an opportunity to provide vertical profiles for many molecules for almost the same air mass.

The final product of those measurements is presented in several papers concerning atmospheric chemistry [113–116]. Analysis of all the flight data is an ongoing process, where post-flight characterization of the SIR (for example, precise laboratory measurement of the SIR sideband ratio) gave a new input to the processing of the flight data with higher accuracy. Already analyzed data proved the SIR to be one of the most sensitive sub-THz spectrometers, allowing us to measure concentrations of trace gases lower than 1 ppbv.

In summary, the capability of the Superconducting Integrated Receiver for high resolution atmospheric spectroscopy has been successfully proven during four scientific balloon flights. During these missions, the phase-locked SIR operation and frequency switching in the 480–650 GHz frequency range has been realized. An intrinsic spectral resolution of the SIR well below 1 MHz has been confirmed by CW signal measurements in the laboratory. An uncorrected double-sideband noise temperature below 120 K has been measured for the SIR when operated with a phase-locked FFO at an intermediate frequency bandwidth of 4–8 GHz. To ensure remote operation of the phase-locked SIR, several software procedures for automatic control have been developed and tested. The first tentative HCl profile has been presented, and its quality

looks promising for future data reduction. Diurnal cycles of ClO and BrO have been observed at different viewing configurations (altitude), with a BrO line level of only approximately 0.5 K [16, 17, 19, 21].

The Superconducting Integrated Receiver can be considered as an operational device that is ready for many applications. The high sensitivity and spectral resolution of the integrated spectrometer enables the analysis of multi-component gas mixtures. Possibilities to use the SIR devices for analysis of exhaled air in medical surveys have been demonstrated [16, 19]. Recently the SIR was successfully implemented for the first spectral measurements of THz radiation emitted from intrinsic Josephson junction stacks (BSCCO mesa) at frequencies up to 750 GHz [17, 117]. Application of the SIR has allowed us to measure radiation emitted from intrinsic Josephson junction stacks in both regimes with a spectral resolution better than 1 MHz for the first time [117]. While at low bias, we found that linewidth is not smaller than 500 MHz, at high bias, the emission linewidth turned out to be in the range of 10–100 MHz. We attribute this to the hot spot acting as a synchronizing element; a linewidth as narrow as 7 MHz has been recorded at high bias. The phase-locked SIR has been used for the locking of the BSCCO oscillator during the test [17]. This first successful attempt to phase-lock a BSCCO oscillator to a stable microwave reference opens up prospects for its practical application.

7.4 Conclusions

The extremely high characteristic frequency, unique nonlinearity and very low intrinsic noise of niobium-based tunnel nanostructures, caused by their nature and cryogenic-operating temperatures, provide the possibility of developing unbeaten THz range detectors. The SIS mixers are certainly the best input devices in the sub-THz range; their noise temperatures are limited only by quantum effects. The technology of high-quality Nb-based tunnel junctions that were developed at Kotelnikov IREE primarily for the fabrication of low-noise SIS receivers, has been successfully used for a number of physical experiments in quite different areas. For example,

the developed technology was implemented in the fabrication of superconducting metamaterials [118–120].

We proposed and developed the superconducting integrated receiver (SIR) that comprises in a single chip a planar antenna combined with a superconductor-insulator-superconductor (SIS) mixer, a superconducting flux-flow oscillator (FFO) acting as a local oscillator (LO), and a second SIS harmonic mixer (HM) for the FFO phase-locking. Improving on the fully Nb-based SIR, we developed and studied Nb–AlN–NbN circuits that exhibit extended operation frequency ranges. Continuous tuning of the phase-locked FFO was experimentally demonstrated at any frequency in the range of 250–750 GHz. The FFO free-running linewidth was measured as being between 1 and 5 MHz, which allows us to phase-lock up to 97% of the emitted FFO power. The output power of the FFO is sufficient to pump the matched SIS mixer. These achievements enabled the development of a 480–650 GHz integrated receiver for the atmospheric-research instrument TELIS (TErahertz and submillimeter Limb Sounder). We demonstrated for the first time the capabilities of the SIR technology for heterodyne spectroscopy in general, and atmospheric limb sounding in particular. At present, the SIR is probably the most functionally complex fully superconducting device that was already successfully implemented in practical applications. New techniques for the fabrication of high-quality SIS tunnel junctions with a gap voltage $V_g > 5$ mV, as well as an approach for phase-locking of the cryogenic oscillators with linewidths up to 50 MHz [17, 121], have been developed to extend the operation frequency of the SIR beyond 1 THz.

Acknowledgment

The authors thank the following colleagues for their support, help, and assistance in the development of the SIR technology: A Baryshev, A. B. Ermakov, M. I. Faley, H. Golstein, A. Golubov, T. de Graauw, L. de Jong, K. V. Kalashnikov, A. V. Khudchenko, N. V. Kinev, O. S. Kiselev, J. Kooi, M. Yu. Kupriyanov, A. de Lange, G. de Lange, I. L. Lapitskay, A. L. Pankratov, D. G. Paveliev, O. M. Pylypenko, K. I. Rudakov, S. V. Shitov, M. Yu. Torgashin, A. V. Ustinov, V. L. Vaks, H. Wang, W. Wild, and P. Yagoubov.

References

1. Tucker, J. R. (1979). Quantum limited detection in tunnel junction mixers. *IEEE J. Quantum Electron.*, **15**, 1234–1258.
2. Tucker, J. R., and Feldman, M. J. (1985). Quantum detection at millimeter wavelengths. *Rev. Mod. Phys.*, **57**, 1055–1113.
3. Kooi, J. W., Chan, M., Phillips, T. G., Bumble, B., and Leduc, H. G. (1992). A low noise 230 GHz heterodyne receiver employing a $0.25 \mu\text{m}^2$ Nb/AlO_x/Nb tunnel junction. *IEEE Trans. Microwave Theory Tech.*, **40**, 812–815.
4. Karpov, A., Blondell, J., Voss, M., and Gundlach, K. H. (1995). Four photons sensitivity heterodyne detection of submillimeter radiation with superconducting tunnel junctions. *IEEE Trans. Appl. Supercond.*, **5**, 3304–3307.
5. Gaidis, M. C., Leduc, H. G., Bin, M., Miller, D., Stern, J. A., and Zmuidzinis, J. (1996). Characterization of low noise quasi-optical SIS mixers for the submillimeter band. *IEEE Trans. Microwave Theory Tech.*, **44**, 1130–1139.
6. Baryshev, A. M. (2005). Superconductor-insulator-superconductor THz mixer integrated with a superconducting flux-flow oscillator. PhD thesis, Delft University of Technology, ISBN 90-9019220-4.
7. Jackson, B. D., de Lange, G., Zijlstra, T., Kroug, M., Klapwijk, T. M., and Stern, J. A. (2005). Niobium titanium nitride-based superconductor-insulator-superconductor mixers for low-noise terahertz receivers. *J. Appl. Phys.*, **97**, 113904.
8. de Graauw, Th., Whyborn, N., Caux, E., Phillips, T. G., Stutzki, J., Tielens, X., Güsten, R., Helmich, F. P., Luinge, W., Pearson, J., Roelfsema, P., Schieder, R., Wildeman, K., and Wavelbakker, K. (2006). The Herschel-heterodyne instrument for the far-infrared (HIFI). Available at: herschel.esac.esa.int/Publ/2006/SPIE2006_HIFI_paper.pdf
9. de Lange, G., Jackson, B. D., Jochemsen, M., Laauwen, W. M., De Jong, L., Kroug, M., Zijlstra, T., and Klapwijk, T. M. (2006). Performance of the flight model HIFI band 3 and 4 mixer units. *Proc. SPIE*, **6275**, 627517.
10. Honigh, C. E., Haas, S., Hottgenroth, D., Jacobs, K., and Stutzki, J. (1997). Low-noise broadband fixed tuned wave-guidemixers at 660 and 800 GHz. *IEEE Appl. Phys.*, **7**(2), 2582–2586.
11. Kooi, J. W., Kovács, A., Sumner, M. C., Chattopadhyay, G., Ceria, R., Miller, D., Bumble, B., Le Duc, R., Stern, J. A., and Phillips, T. G. (2007). A 275–425 GHz tunerless waveguide receiver based on AlN SIS technology. *IEEE Trans. Microwave Theory Tech.*, **55**(10), 2086–2096.

12. Kooi, J. W. (2008). Advanced receivers for submillimeter and far infrared astronomy. PhD thesis, Groningen State University, ISBN 978-90-367-3653-4.
13. Uzawa, Y., Fujii, Y., Gonzalez, A., Kaneko, K., Kroug, M., Kojima, T., Miyachi, A., Makise, K., Saito, S., Terai, H., and Wang, Z. (2015). Tuning circuit material for mass-produced terahertz SIS receivers. *IEEE Trans. Appl. Supercond.*, **25**(3), 2401005.
14. Koshelets, V. P., Shitov, S. V., Filippenko, L. V., Baryshev, A. M., Golstein, H., de Graauw, T., Luinge, W., Schaeffer, H., and van de Stadt, H. (1996). First implementation of a superconducting integrated receiver at 450 GHz. *Appl. Phys. Lett.*, **68**, 1273.
15. Koshelets, V. P., and Shitov, S. V. (2000). Integrated superconducting receivers. *Supercond. Sci. Technol.*, **13**, R53–R69.
16. Koshelets, V. P., Birk, M., Boersma, D., Dercksen, J., Dmitriev, P. N., Ermakov, A. B., Filippenko, L. V., Golstein, H., Hoogeveen, R., de Jong, L., Khudchenko, A. V., Kinev, N. V., Kiselev, O. S., Kudryashov, P. V., van Kuik, B., de Lange, A., de Lange, G., Lapitsky, I. L., Pripolzin, S. I., van Rantwijk, J., Selig, A., Sobolev, A. S., Torgashin, M. Yu., Vaks, V. L., de Vries, E., Wagner, G., and Yagoubov, P. A. (2011). Integrated submm wave receiver: development and applications, in *Nanoscience Frontiers - Fundamentals of Superconducting Electronics*, ed. Sidorenko, A. Springer Series: NanoScience and Technology (Springer Berlin Heidelberg), pp. 263–296.
17. Koshelets, V. P., Dmitriev, P. N., Faley, M. I., Filippenko, L. V., Kalashnikov, K. V., Kinev, N. V., Kiselev, O. S., Artanov, A. A., Rudakov, K. I., de Lange, A., de Lange, G., Vaks, V. L., Li, M. Y., and Wang, H. B. (2015). Superconducting integrated terahertz spectrometers. *IEEE Trans. Terahertz Sci. Technol.*, **5**, 687–694.
18. Koshelets, V. P., Ermakov, A. B., Filippenko, L. V., Khudchenko, A. V., Kiselev, O. S., Sobolev, A. S., Torgashin, M. Yu., Yagoubov, P. A., Hoogeveen, R. W. M., and Wild, W. (2007). Integrated submillimeter receiver for TELIS. *IEEE Trans. Appl. Supercond.*, **17**, 336–342.
19. Koshelets, V. P., Ermakov, A. B., Filippenko, L. V., Kinev, N. V., Kiselev, O. S., Torgashin, M. Yu., de Lange, A., de Lange, G., Pripolzin, S. I., and Vaks, V. L. (2010). *Proc. SPIE*, **7854**, 78540J.
20. de Lange, G., Boersma, D., Dercksen, J., Dmitriev, P. N., Ermakov, A. B., Filippenko, L. V., Golstein, H., Hoogeveen, R., de Jong, L., Khudchenko, A. V., Kinev, N. V., Kiselev, O. S., van Kuik, B., de Lange, A., van Rantwijk, J., Sobolev, A. S., Torgashin, M. Yu., de Vries, E., Yagoubov, P. A., and Koshelets, V. P. (2010). Development and characterization of the

- superconducting integrated receiver channel of the TELIS atmospheric sounder. *Supercond. Sci. Technol.*, **23**(4), 045016 (8pp).
21. Kiselev, O., Birk, M., Ermakov, A., Filippenko, L., Golstein, H., Hoogeveen, R., Kinev, N., van Kuik, B., de Lange, A., de Lange, G., Yagoubov, P., and Koshelets, V. (2011). Balloon-borne superconducting integrated receiver for atmospheric research. *IEEE Trans. Appl. Supercond.*, **21**, 612–615.
 22. Rowell, J. M., Gurvitch, M., and Geerk, J. (1981). Modification of tunneling barriers on Nb by a few monolayers of Al. *Phys. Rev. B*, **24**, 2278–2281.
 23. Gurvitch, M., Washington, W. A., and Huggins, H. A. (1983). High quality refractory Josephson tunnel junctions utilizing thin aluminum layers. *Appl. Phys. Lett.*, **42**, 472–474.
 24. Huggins, H. A., and Gurvitch, M. (1985). Preparation and characteristics of Nb-AlOxide-Nb tunnel junctions. *J. Appl. Phys.*, **57**, 2103–2109.
 25. Kroger, H., Smith, L. N., and Jillie, D. W. (1981). Selective niobium anodisation process for fabrication Josephson tunnel junctions. *Appl. Phys. Lett.*, **39**, 280–282.
 26. Morohashi, S., and Hasuo, S. (1987). Experimental investigations and analysis for high-quality Nb/Al-AlO_x/Nb Josephson junctions. *J. Appl. Phys.*, **61**, 4835–4849.
 27. Morohashi, S., Shinoki, F., Shoji, A., et al. (1985). High quality Nb/Al-AlO_x/Nb Josephson junction. *Appl. Phys. Lett.*, **46**, 2103–2109.
 28. Imamura, T., Shiota, T., and Hasuo, S. (1992). Fabrication of high quality Nb/AlO_x-Al/Nb Josephson junctions: I - Sputtered Nb films for junction electrode. *IEEE Trans. Appl. Supercond.*, **2**, 1.
 29. Imamura, T., and Hasuo, S. (1992). Fabrication of high quality Nb/AlO_x-Al/Nb Josephson junctions: II - Deposition of thin Al layers on Nb layers. *IEEE Trans. Appl. Supercond.*, **2**, 84.
 30. Imamura, T., and Hasuo, S. (1992). Fabrication of high quality Nb/AlO_x-Al/Nb Josephson junctions: III - Annealing stability of AlO_x tunneling barriers. *IEEE Trans. Appl. Supercond.*, **2**, 222.
 31. Dmitriev, P. N., Ermakov, A. B., Kovalenko, A. G., Koshelets, V. P., Iosad, N. N., Golubov, A. A., and Kupriyanov, M. Yu. (1999). Niobium tunnel junctions with multi-layered electrodes. *IEEE Trans. Appl. Supercond.*, **9**, 3970–3973.
 32. Koshelets, V. P., Kovtonyuk, S. A., Serpuchenko, I. L., Filippenko, L. V., and Shchukin, A. V. (1991). High quality Nb-AlO_x-Nb tunnel junctions for microwave and SFQ logic devices. *IEEE Trans. Magn.*, **27**, 3141–3144.

33. Golubov, A. A., Houwman, E. P., Gijsbertsen, J. G., Krasnov, V. M., Lokstra, J. F., Rogalla, H. (1995). Proximity effect in superconductor-insulator-superconductor Josephson tunnel junctions: theory and experiment. *Phys. Rev. B*, **51**, 1073–1089.
34. Shiota, T., Imamura, T., and Hasuo, S. (1992). Nb Josephson junctions with an AlN_x barrier made by plasma nitridation. *Appl. Phys. Lett.*, **61**, 1228–1230.
35. Kleinsasser, A. W., Mallison, W. H., and Miller, R. E. (1995). Nb/AlN/Nb Josephson-junctions with high critical current density. *IEEE Trans. Appl. Supercond.*, **5**, 2318–2321.
36. Kawamura, J., Miller, D., Chen, J., Zmuidzinis, J., Bumble, B., Le Duc, H. G., and Stern, J. A. (2000). Very high-current-density Nb/AlN/Nb tunnel junctions for low-noise submillimeter mixers. *Appl. Phys. Lett.*, **76**, 2119.
37. Bumble, B., Le Duc, H. G., Stern, J. A., and Megerian, K. G. (2001). Fabrication of Nb/AlN_x/NbTiN junctions for SIS mixer applications. *IEEE Trans. Appl. Supercond.*, **11**, 76–79.
38. Iosad, N. N., Ermakov, A. B., Meijer, F. E., Jackson, B. D., and Klapwijk, T. M. (2002). Characterization of the fabrication process Nb/Al-AlN_x/Nb tunnel junctions with low R_nA values up to 1 Ωμm². *Supercond. Sci. Technol.*, **15**, 945–951.
39. Dmitriev, P. N., Lapitskaya, I. L., Filippenko, L. V., Ermakov, A. B., Shitov, S. V., Prokopenko, G. V., Kovtonyuk, S. A., and Koshelets, V. P. (2003). High quality Nb-based tunnel junctions for high frequency and digital applications. *IEEE Trans. Appl. Supercond.*, **13**(2), 107–110.
40. Torgashin, M. Yu., Koshelets, V. P., Dmitriev, P. N., Ermakov, A. B., Filippenko, L. V., and Yagoubov, P. A. (2007). Superconducting integrated receivers based on Nb-AlN-NbN circuits. *IEEE Trans. Appl. Supercond.*, **17**, 379–382.
41. Khudchenko, A., Baryshev, A. M., Rudakov, K., Koshelets, V., Dmitriev, P., Hesper, R., and de Jong, L. (2016). High gap Nb-AlN-NbN SIS junctions for frequency band 790–950 GHz. *IEEE Trans. Terahertz Sci. Technol.*, **6**(1), 127–132.
42. Kasemann, C., Gu'sten, R., Heyminck, S., Klein, B., Klein, T., Philipp, S. D., Korn, A., Schneider, G., Henseler, A., Baryshev, A., and Klapwijk, T. M. (2006). CHAMP+: a powerful array receiver for APEX. *Proc. SPIE*, **6275**, 62750N.
43. Gu'sten, R., Booth, R., Cesarsky, C., and Menten, K., et al., (2006). Ground-based and airborne telescopes. *Proc. SPIE*, **6267**, 626714-1.

44. Smirnov, A. V., Baryshev, A. M., de Bernardis, P., Vdovin, V. F., Goltsman, G. N., Kardashev, N. S., Kuzmin, L. S., Koshelets, V. P., Vystavkin, A. N., Lobanov, Yu. V., Ryabchun, S. A., Finkel, S. A., and Khokhlov, D. R. (2012). The current stage of development of the receiving complex of the Millimeter space observatory. *Radiophys. Quantum Electron.*, **54**(8–9), 557–568.
45. Zmuidzinas, J., LeDuc, H. G., Stern, J. A., and Cypher, S. R. (1994). Two-junction tuning circuits for submillimeter SIS mixers. *IEEE Trans. Microwave Theory Tech.*, **42**(4), 698–706.
46. Belitsky, V. Yu., Jacobsson, S. W., Filippenko, L. V., and Kollberg, E. L. (1995). Broadband twin-junction tuning circuit for submillimeter SIS mixers. *Microwave. Opt. Technol. Lett.*, **10**, 74–78.
47. Shoji, A., Kosaka, S., Shinoki, F., Aoyagi, M., and Hayakawa, H. (1983). All refractory Josephson tunnel junctions fabricated by reactive ion etching. *IEEE Trans. Magn.*, **19**, 827–830.
48. Shoji, A., Aoyagi, M., Kosaka, S., Shinoki, F., and Hayakawa, H. (1985). Niobium nitride Josephson tunnel junctions with magnesium oxide barriers. *Appl. Phys. Lett.*, **46**, 1098–1100.
49. Blaugher, R. D., Przybysz, J. X., Talvacchio, J., and Battyan, J. (1987). Processing of all-NbN tunnel junction series arrays. *IEEE Trans. Magn.*, **23**(2), 673–675.
50. Talvacchio, J., and Braginski, A. I. (1987). Tunnel junctions fabricated from coherent NbN/MgO/NbN and NbN/Al₂O₃/NbN structures. *IEEE Trans. Magn.*, **23**, 859–862.
51. Wang, Z., Uzawa, Y., and Kawakami, A. (1997). High current density NbN/AlN/NbN tunnel junctions for submillimeter wave SIS mixers. *IEEE Trans. Appl. Supercond.*, **7**(2), 2797–2800.
52. Uzawa, Y., Wang, Z., and Kawakami, A. (1998). Terahertz NbN/AlN/NbN mixers with Al/SiO/NbN microstrip tuning circuits. *Appl. Phys. Lett.*, **73**(5), 680–682.
53. Wang, Z., Terai, H., Kawakami, A., and Uzawa, Y. (1999). Interface and tunneling barrier heights of NbN/AlN/NbN tunnel junctions. *Appl. Phys. Lett.*, **75**, 701.
54. Wang, Z., Terai, H., Qiu, W., Makise, K., Uzawa, Y., Kimoto, K., and Nakamura, Y. (2013). High-quality epitaxial NbN/AlN/NbN tunnel junctions with a wide range of current density. *Appl. Phys. Lett.*, **102**(14), 142604-1–142604-5.
55. Zijlstra, T., Lodewijk, C. F. J., Vercruyssen, N., Tichelaar, F. D., Loudkov, D. N., and Klapwijk, T. M. (2007). Epitaxial aluminum nitride tunnel

- barriers grown by nitridation with a plasma source. *Appl. Phys. Lett.*, **91**, 233102–233105.
56. Josephson, B. D. (1962). Possible new effects in superconductive tunneling. *Phys. Lett.*, **1**, 251–253.
 57. Josephson, B. D. (1964). Coupled superconductors. *Rev. Mod. Phys.*, **36**, 216–220.
 58. Likharev, K. K. (1986). *Dynamics of Josephson Junctions and Circuits*, Gordon and Breach: London.
 59. Varmazis, C., Sandell, R. D., Jain, A. K., and Lukens, J. E. (1978). Generation of coherent tunable Josephson radiation at microwave frequencies with narrowed linewidth. *Appl. Phys. Lett.*, **33**, 357.
 60. Jain, A. K., Likharev, K. K., Lukens, J. E., and Sauvageau, J. E. (1984). Mutual phase-locking in Josephson junction arrays. *Phys. Rep.*, **109**, 309–426.
 61. Dueholm, B., Levring, O. A., Mygind, J., Pedersen, N. F., Soerensen, O. H., and Cirillo, M. (1981). Multisoliton excitations in long Josephson junctions. *Phys. Rev. Lett.*, **46**, 1299.
 62. Joergensen, E., Koshelets, V. P., Monaco, R., Mygind, J., Samuelsen, M. R., and Salerno, M., (1982). Thermal fluctuations in resonant motion of fluxon on a Josephson transmission line: theory and experiment. *Phys. Rev. Lett.*, **49**, 1093–1096.
 63. Cirillo, M., and Lloyd, F. (1987). Phase lock of a long Josephson junction to an external microwave source. *J. Appl. Phys.*, **61**, 2581.
 64. Booi, P. A. A., and Benz, S. P. (1994). Emission linewidth measurements of two-dimensional array Josephson oscillators. *Appl. Phys. Lett.*, **64**, 2163.
 65. Barbara, P., Cawthorne, A. B., Shitov, S. V., and Lobb, C. J. (1999). Stimulated emission and amplification in Josephson junction arrays. *Phys. Rev. Lett.*, **82**, 1963–1965.
 66. Salez, M., and Boussaha, F. (2010). Fluxon modes and phase-locking at 600 GHz in superconducting tunnel junction nonuniform arrays. *J. Appl. Phys.*, **107**, 013908.
 67. Song, F., Müller, F., Scheller, T., Semenov, A. D., He, M., Fang, L., Hübers, H.-W., and Klushin, A. M. (2011). Compact tunable subterahertz oscillators based on Josephson junctions. *Appl. Phys. Lett.*, **98**, 142506.
 68. Galin, M. A., Klushin, A. M., Kurin, V. V., Seliverstov, S. V., Finkel, M. I., Goltsman, G. N., Müller, F., Scheller, T., and Semenov, A. D. (2015). Towards local oscillators based on arrays of niobium Josephson junctions. *Supercond. Sci. Technol.*, **28**, 055002 (7pp).

69. Nagatsuma, T., Enpuku, K., Irie, F., and Yoshida, K. (1983). Flux-flow type Josephson oscillator for millimeter and submillimeter wave region. *J. Appl. Phys.*, **54**, 3302.
70. Nagatsuma, T., Enpuku, K., Sueoka, K., Yoshida, K., and Irie, F. (1984). Flux-flow type Josephson oscillator for millimeter and submillimeter wave region. II. Modeling. *J. Appl. Phys.*, **56**, 3284.
71. Nagatsuma, T., Enpuku, K., Yoshida, K., and Irie, F. (1985). Flux-flow type Josephson oscillator for millimeter and submillimeter wave region. III. Oscillation stability. *J. Appl. Phys.*, **58**, 441.
72. Qin, J., Enpuku, K., and Yoshida, K. (1988). Flux-flow type Josephson oscillator for millimeter and submillimeter wave region. IV. Thin-film coupling. *J. Appl. Phys.*, **63**, 1130.
73. Zhang, Y. M., and Wu, P. H. (1990). Numerical calculation of the height of velocity-matching step of flux-flow type Josephson oscillator. *J. Appl. Phys.*, **68**, 4703–4709.
74. Zhang, Y. M., Winkler, D., and Claeson, T. (1993). Detection of mm and submm wave radiation from soliton and flux-flow modes in a long Josephson junction. *IEEE Trans. Appl. Supercond.*, **3**, 2520–2523.
75. Koshelets, V. P., Dmitriev, P. N., Ermakov, A. B., Sobolev, A. S., Torgashin, M. Yu., Kurin, V. V., Pankratov, A. L., Mygind, J. (2005). Optimization of the phase-locked flux-flow oscillator for the submm integrated receiver. *IEEE Trans. Appl. Supercond.*, **15**, 964–967.
76. Koshelets, V. P., Shitov, S. V., Shchukin, A. V., Filippenko, L. V., Mygind, J., and Ustinov, A. V. (1997). Self-pumping effects and radiation linewidth of Josephson flux flow oscillators. *Phys. Rev. B*, **56**, 5572–5577.
77. Koshelets, V. P., Shitov, S. V., Shchukin, A. V., Filippenko, L. V., and Mygind, J., (1996). Linewidth of submillimeter wave flux-flow oscillators. *Appl. Phys. Lett.*, **69**, 699–701.
78. Koshelets, V. P., Shitov, S. V., Shchukin, A. V., Filippenko, L. V., Dmitriev, P. N., Vaks, V. L., Mygind, J., Baryshev, A. M., Luinge, W., and Golstein, H. (1999). Flux flow oscillators for sub-mm wave integrated receivers. *IEEE Trans. Appl. Supercond.*, **9**, 4133–4136.
79. Koshelets, V. P., and Mygind, J., (2001). Flux flow oscillators for superconducting integrated submm wave receivers, in *Studies of High Temperature Superconductors*, ed. Narlikar, A. V., NOVA Science Publishers: New York, **39**, pp. 213–244.
80. Koshelets, V. P., Ermakov, A. B., Dmitriev, P. N., Sobolev, A. S., Baryshev, A. M., Wesselius, P. R., and Mygind, J. (2001). Radiation linewidth of flux flow oscillators. *Supercond. Sci. Technol.*, **14**, 1040–1043.

81. Koshelets, V. P., Shitov, S. V., Filippenko, L. V., Vaks, V. L., Mygind, J., Baryshev, A. B., Luinge, W., and Whyborn, N. (2000). Phase locking of 270-440 GHz Josephson flux flow oscillator. *Rev. Sci. Instrum.*, **71**(1), 289–293.
82. Berberich, H., Buemann, R., and Kinder, H. (1982). Monochromatic phonon generation by the Josephson effect. *Phys. Rev. Lett.*, **49**, 1500.
83. Kinder, H., Berberich, P., and Schick, A. (1984). High resolution phonon spectroscopy using the Josephson effect. *Physica B+C*, **127**, 210–213.
84. Ehre, D., Lyahovitskaya, V., Tagantsev, A., and Lubomirsky, I. (2007). Amorphous piezo- and pyroelectric phases of BaZrO₃ and SrTiO₃. *Adv. Mater.*, **19**, 1515–1517.
85. Schlomann, E. (1964). Dielectric losses in ionic crystals with disordered charge distributions. *Phys. Rev.*, **135**, A413–A419.
86. Kozub, V. I. (1983). Possible explanation of monochromatic phonon emission by the Josephson junction. *Phys. Rev. Lett.*, **51**, 1498.
87. Werthamer, N. R. (1966). Nonlinear self-coupling of Josephson radiation in superconducting tunnel junctions. *Phys. Rev.*, **147**, 255–263.
88. Hasselberg, L.-E., Levinsen, M. T., and Samuelsen, M. R. (1974). Theories of subharmonic gap structures in superconducting junctions. *Phys. Rev. B*, **9**, 3757–3765.
89. Tredwell, T. J., and Jacobsen, E. H. (1975). Phonon-induced enhancement of the superconducting energy gap. *Phys. Rev. Lett.*, **35**, 244–246; Tredwell, T. J., and Jacobsen, E. H. (1976). Phonon-induced increase in the energy gap of superconducting films. *Phys. Rev. B*, **13**, 2931–2942.
90. Volodin, A. P., Logvenov, G. Yu., Ryazanov, V. V., and Fal'kovskii, I. V. (1987). Acoustoelectric effect at a Josephson SNS junction. *Sov. Phys. JETP Lett.*, **46**, 48–51.
91. Schlenga, K., Hechtfischer, G., Kleiner, R., Walkenhorst, W., and Müller, P. (1996). Subgap structures in intrinsic Josephson junctions of Tl₂Ba₂Ca₂Cu₃O_{10+δ} and Bi₂Sr₂CaCu₂O_{8+δ}. *Phys. Rev. Lett.*, **76**, 4943–4946.
92. Yurgens, A., Winkler, D., Zavaritsky, N., and Claeson, T. (1996). Gap and sub-gap structures of intrinsic Josephson tunnel junctions in Bi₂Sr₂CaCu₂O_x single crystals. *Proc. SPIE*, **2697**, 433–451.
93. Helm, Ch., Preis, Ch., Forsthofer, F., Keller, J., Schlenga, K., Kleiner, R., and Müller, P. (1997). Coupling between phonons and intrinsic Josephson oscillations in cuprate superconductors. *Phys. Rev. Lett.*, **79**, 737–740.

94. Krasnov, V. M. (2006). Quantum cascade phenomenon in $\text{Bi}_2\text{Sr}_2\text{CaCu}_2\text{O}_{8+\delta}$ single crystals. *Phys. Rev. Lett.*, **97**, 257003(1–4).
95. Maksimov, E. G., Arseev, P. I., and Maslova, N. S. (1999). Phonon assisted tunneling in Josephson junctions. *Solid State Commun.*, **111**, 391–395.
96. Helm, Ch., Preis, Ch., Walter, Ch., and Keller, J. (2000). Theory for the coupling between longitudinal phonons and intrinsic Josephson oscillations in layered superconductors. *Phys. Rev. B*, **62**, 6002–6014.
97. Katterwe, S.-O., Motzkau, H., Rydh, A., and Krasnov, V. M. (2011). Coherent generation of phonon-polaritons in $\text{Bi}_2\text{Sr}_2\text{CaCu}_2\text{O}_{8+x}$ intrinsic Josephson junctions. *Phys. Rev. B*, **83**, 100510R (1–4).
98. Koshelets, V. P., Ermakov, A. B., Shitov, S. V., Dmitriev, P. N., Filippenko, L. V., Baryshev, A. M., Luinge, W., Mygind, J., Vaks, V. L., and Pavel'ev, D. G. (2001). Superfine resonant structure on IVC of long Josephson junctions and its influence on flux flow oscillator linewidth. *IEEE Trans. Appl. Supercond.*, **11**, 1211–1214.
99. Koshelets, V. P. (2014). Subterahertz sound excitation and detection by long Josephson junction. *Supercond. Sci. Technol.*, **27**, 065010 (7pp).
100. Eisenmenger, W., and Dayem, A. H. (1967). Quantum generation and detection of incoherent phonons in superconductors. *Phys. Rev. Lett.*, **18**, 125–127.
101. Eisenmenger, W. (1976). Superconducting tunnel junctions as phonon generators and detectors, in *Physical Acoustics: Principles and Methods*, Academic Press: New York, pp. 79–153.
102. Bron, W. E. (1980). Spectroscopy of high-frequency phonons. *Rep. Prog. Phys.*, **43**, 301–352.
103. Ivanchenko, Yu. M., and Medvedev, Yu. V. (1971). Excitation of sound in a Josephson junction. *Sov. Phys. JETP*, **33**, 1223–1228.
104. McSkimin, H. J., and Andreatch, P. (1964). Elastic moduli of silicon vs hydrostatic pressure at 25.0°C and –195.8°C. *J. Appl. Phys.*, **35**, 2161–2165.
105. Teichert, C., MacKay, J. F., Savage, D. E., Lagally, M. G., Brohl, M., and Wagner, P. (1995). Comparison of surface roughness of polished silicon wafers measured by light scattering topography, soft x-ray scattering, and atomic force microscopy. *Appl. Phys. Lett.*, **66**, 2346–2348.
106. Polzikova, N. I., Mansfeld, G. D., Tokpanov, Y. S., and Koshelets, V. P. (2011). Resonant subterahertz coherent acoustic waves excitation by Josephson junction. *Proc. 2011 Joint Conference of the IEEE International Frequency Control Symposium & European Frequency and Time Forum*, ISSN: 1075–6787, 483–485.

107. <http://vadiodes.com/index.php/en/products/full-band-multipliers-wr-series>
108. <http://www.almaobservatory.org/en/about-alma/how-does-alma-work/technology/front-end>
109. Hoogeveen, R. W. M., Yagoubov, P. A., de Lange, A., Selig, A. M., Koshelets, V. P., Ellison, B. N., and Birk, M. (2005). *Proc. SPIE*, **5978**, 440.
110. Hoogeveen, R. W. M., Yagoubov, P. A., de Lange, G., de Lange, A., Koshelets, V., Birk, M., and Ellison, B. (2007). *Proc. SPIE*, **6744**, 67441U-1.
111. Friedl-Vallon, F., Maucher, G., Seefeldner, M., Trieschmann, O., Kleinert, A., Lengel, A., Keim, C., Oelhaf, H., and Fischer, H. (2004). *Appl. Opt.*, **43**, 3335.
112. Sobis, P., Drakinskiy, V., Wadefalk, N., Karandikhar, Y., Hammar, A., Emrich, A., Zhao, H., Bryllert, T., Tang, A.-Y., Nilsson, P.-Å., Schlee, J., Kim, H., Jacob, K., Murk, A., Grahn, J., and Stake, J. (2014). Low noise GaAs Schottky TMIC and InP Hemt MMIC based receivers for the ISMAR and SWI instruments. Micro-and Millimetre Wave Technology and Techniques Workshop 2014, ESA-ESTEC, Noordwijk, The Netherlands.
113. de Lange, A., Birk, M., de Lange, G., Friedl-Vallon, F., Kiselev, O., Koshelets, V., Maucher, G., Oelhaf, H., Selig, A., Vogt, P., Wagner, G., and Landgraf, J. (2012). HCl and ClO in activated Arctic air; first retrieved vertical profiles from TELIS submillimetre limb spectra. *Atmos. Meas. Tech.*, **5**, 487–500.
114. Xu, J., Schreier, F., Vogt, P., Doicu, A., and Trautmann, T. (2013). A sensitivity study for far infrared balloon-borne limb emission sounding of stratospheric trace gases. *Geosci. Instrum. Methods Data Syst. Discuss.*, **3**, 251–303.
115. Kasai, Y., Sagawa, H., Kreyling, D., Dupuy, E., Baron, P., Mendrok, J., Suzuki, K., Sato, T. O., Nishibori, T., Mizobuchi, S., Kikuchi, K., Manabe, T., Ozeki, H., Sugita, T., Fujiwara, M., Irimajiri, Y., Walker, K. A., Bernath, P. F., Boone, C., Stiller, G., von Clarmann, T., Orphal, J., Urban, J., Murtagh, D., Llewellyn, E. J., Degenstein, D., Bourassa, A. E., Lloyd, N. D., Froidevaux, L., Birk, M., Wagner, G., Schreier, F., Xu, J., Vogt, P., Trautmann, T., and Yasui, M. (2013). Validation of stratospheric and mesospheric ozone observed by SMILES from International Space Station. *Atmos. Meas. Tech.*, **6**, 2311–2338.
116. Sagawa, H., Sato, T., Baron, P., Dupuy, E., Livesey, N., Urban, J., von Clarmann, T., de Lange, A., Wetzell, G., Kagawa, A., Murtagh, D., and

- Kasai, Y. (2013). Comparison of SMILES CIO profiles with other satellite and balloon-based measurements. *Atmos. Meas. Tech. Discuss.*, **6**(1), 613–663.
117. Li, M., Yuan, J., Kinev, N., Li, J., Gross, B., Gu'eron, S., Ishii, A., Hirata, K., Hatano, T., Koelle, D., Kleiner, R., Koshelets, V. P., Wang, H., and Wu, P. (2012). Linewidth dependence of coherent terahertz emission from $\text{Bi}_2\text{Sr}_2\text{CaCu}_2\text{O}_8$ intrinsic Josephson junction stacks in the hot-spot regime. *Phys. Rev. B*, **86**, 060505(R).
118. Butz, S., Jung, P., Filippenko, L. V., Koshelets, V. P., and Ustinov, A. V. (2013). A one-dimensional tunable magnetic metamaterial. *Opt. Express*, **21**(19), 22540–22548.
119. Vidiborskiy, A., Koshelets, V. P., Filippenko, L. V., Shitov, S. V., and Ustinov, A. V. (2013). Ultra-compact tunable split-ring resonators. *Appl. Phys. Lett.*, **103**, 162602.
120. Jung, P., Butz, J., Marthaler, M., Fistul, M. V., Leppäkangas, J., Koshelets, V. P., and Ustinov, A. V. (2014). A multi-stable switchable metamaterial. *Nat. Commun.*, **5**, 3730.
121. Kalashnikov, K. V., Khudchenko, A. V., and Koshelets, V. P. (2013). Harmonic phase detector for phase locking of cryogenic terahertz oscillator. *Appl. Phys. Lett.*, **103**, 102601-1–102601-4.